Nanoscale
Horizons

ROYAL SOCIETY
OF CHEMISTRY

REVIEW

View Article Online
View Journal | View Issue

Check for updates

Cite this: *Nanoscale Horiz.*, 2023, **8**, 716

Memristor-based neural networks: a bridge from device to artificial intelligence

Zelin Cao,[ab] Bai Sun,*[a] Guangdong Zhou,[c] Shuangsuo Mao,[d] Shouhui Zhu,[e] Jie Zhang,[f] Chuan Ke,[f] Yong Zhao[def] and Jinyou Shao*[a]

Received 16th November 2022,
Accepted 7th March 2023

DOI: 10.1039/d2nh00536k

rsc.li/nanoscale-horizons

Since the beginning of the 21st century, there is no doubt that the importance of artificial intelligence has been highlighted in many fields, among which the memristor-based artificial neural network technology is expected to break through the limitation of von Neumann so as to realize the replication of the human brain by enabling strong parallel computing ability and efficient data processing and become an important way towards the next generation of artificial intelligence. A new type of nanodevice, namely memristor, which is based on the variability of its resistance value, not only has very important applications in nonvolatile information storage, but also presents obsessive progressiveness in highly integrated circuits, making it one of the most promising circuit components in the post-Moore era. In particular, memristors can effectively simulate neural synapses and build neural networks; thus, they can be applied for the preparation of various artificial intelligence systems. This study reviews the research progress of memristors in artificial neural networks in detail and highlights the structural advantages and frontier applications of neural networks based on memristors. Finally, some urgent problems and challenges in current research are summarized and corresponding solutions and future development trends are put forward.

---

[a] *Frontier Institute of Science and Technology (FIST), Xi'an Jiaotong University, Xi'an, Shaanxi 710049, China. E-mail: baisun@xjtu.edu.cn, jyshao@xjtu.edu.cn*
[b] *Shaanxi International Joint Research Center for Applied Technology of Controllable Neutron Source, School of Science, Xijing University, Xi'an 710123, China*
[c] *College of Artificial Intelligence, Brain-inspired Computing & Intelligent Control of Chongqing Key Lab, Southwest University, Chongqing 400715, China*
[d] *Fujian Provincial Collaborative Innovation Center for Advanced High-Field Superconducting Materials and Engineering, Fujian Normal University, Fuzhou, Fujian 350117, China*
[e] *School of Physical Science and Technology, Key Laboratory of Advanced Technology of Materials, Southwest Jiaotong University, Chengdu, Sichuan 610031, China*
[f] *School of Electrical Engineering, Southwest Jiaotong University, Chengdu, Sichuan 610031, China*

Zelin Cao

Zelin Cao received his MS degree in Condensed Matter Physics from Southwest Jiaotong University (China) in 2020 and is working at Xijing University (China) since 2021. Currently, his main research interests are the design and manufacture of nanomaterials for memristive memory applications and understanding the microscopic mechanisms of resistance-switching using density functional theory (DFT) calculations.

Bai Sun

Dr Bai Sun received his PhD degree from the Faculty of Materials and Energy, Southwest University (China) in 2015 and worked at Southwest Jiaotong University since 2016. Subsequently, he conducted postdoctoral research at the University of Waterloo (Canada) from 2018 to 2021. Currently, he is a professor at Xi'an Jiaotong University. His research interests mainly focus on the development of new energy materials, preparation of memristive devices and their application in brain-like chips, neural synapses, neural networks, neuromorphic computing, quantum computing, information sensing, electronic skin, artificial intelligence, etc.

1. Introduction

1.1 Memristor

In 1971, Chua believed that there should be a circuit component that can reveal the relationship between the magnetic flux and the charge,[1] which was defined as a memristor. Thus, the memristor, also known as a memory resistor, is considered the fourth fundamental passive circuit component other than the resistor, capacitor, and inductor. The resistance values of the memristor can be continuously adjusted under an applied voltage, and its resistance states are determined by the flowing current or applied voltage. According to the relationship between the four basic variables: voltage (v), current (i), charge (q) and flux (φ) (Fig. 1a), the functional relationship between charge and flux is derived as $M = \mathrm{d}\varphi/\mathrm{d}q$. Here, the charge is the integral of current over time, which can be expressed as $\mathrm{d}q = i\mathrm{d}t$. The flux is the integral of electromotive force or voltage over time, and it can be expressed as $\mathrm{d}\varphi = v\mathrm{d}t$. Hence, memristance can be deduced as $M = v\mathrm{d}t/i\mathrm{d}t = v/i$. According to Ohm's law, the memristance (M) at time t_0 is determined by the accumulation of electric charge in the time period from the initial time to t_0. Therefore, a memristor is a kind of resistive device with nonlinear resistance values in theory. However, for a long time after the memristive theory was proposed, the existence of memristor was not experimentally proven. In 2008, Strukov *et al.* linked the memristive theory with an experimental phenomenon in a double-layer TiO_2 thin-film-based device,[2] in which a hysteresis loop appeared under an applied bias voltage, which is the first proof of the existence of the memristor (Fig. 1b). Since then, memristive technologies have flourished, ranging from material systems and physical mechanisms to advanced algorithms.

The resistance values of a memristor can be changed under an applied voltage or current, that is, it can memorize the flowing current in the device by changing its resistance states. The most common structure of a memristor is a sandwich composed of metal/insulator/metal layers. The top and bottom metal layers are used as the top electrode and the bottom electrode, respectively, and the middle layer is used as the functional layer of the memristive device. The memristor usually exhibits a zero-crossing current–voltage (I–V) hysteresis loop arising from the resistive switching characteristics. Under the action of an external electric field (direct current or pulse signal), the memristor can undergo a reversible transition between the high-resistance state (HRS) and the low-resistance state (LRS), as shown in Fig. 1c. The conductance of the memristor increases under the action of the applied voltage, which is known as the SET process, while it is called the RESET process when the conductance decreases under the action of reversed voltage.[3–5] Depending on the polarity of the switching voltage, memristors can be divided into bipolar and unipolar resistive switching devices.[6] The direction of bipolar resistive switching relies on the polarity of the applied voltage, while the

Guangdong Zhou

Dr Guangdong Zhou received his PhD degree from the Faculty of Materials and Energy, Southwest University (China) in 2018. He conducts his postdoctoral research at Southwest University. His research focus is on the physical mechanisms of memristors and memristor-based functions, including memory logics, displays and synapses. His memristor-related research is supported by the Postdoctoral Program for Innovative Talent Support of Chongqing. In the past 10 years, he has published more than 80 peer-reviewed papers.

Shuangsuo Mao

Shuangsuo Mao is pursuing his PhD Degree at the College of Physics and Energy, Fujian Normal University (China). He received an M.S. degree in Condensed Matter Physics from Southwest Jiaotong University in 2020. His research focus is on the design of memristive devices and the fabrication of nanomaterials for memory applications.

Jinyou Shao

Dr Jinyou Shao received his PhD degree from Xi'an Jiaotong University, Xi'an, China, in 2009. He is currently a professor at the State Key Laboratory for Manufacturing Systems Engineering, Xi'an Jiaotong University. His research interests include micro/nanomanufacturing techniques, flexible electronics and systems, nanosensors and devices. Prof. Shao received the First Prize Technology Invention Award from the Ministry of Education of China in 2015. He has been awarded Changjiang Scholars –Young Category, NSFC Fund for Excellent Young Scholars, New Century Excellent Talents by MoE of China, Shaanxi Young Talents in Science and Technology, ACS Membership Award, etc.

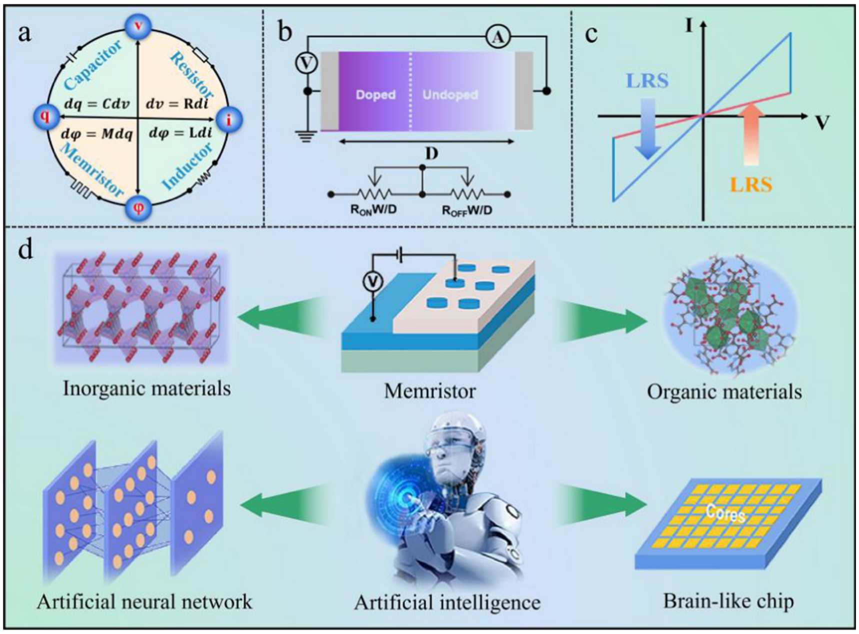

Fig. 1 (a) Schematic of the relationship between the four basic circuit components. (b) The coupled variable-resistor effect of a memristive device based on the TiO_2 film. Panel b is reproduced with permission.[2] Copyright 2008, Nature Publishing Group. (c) The hysteretic I–V characteristic curve corresponding to the resistive switching effect. (d) Schematic of the memristor, in which the functional layer is made of inorganic and organic materials, used to build neural networks for artificial intelligence and brain-like chips.

direction of unipolar resistive switching is only determined by the applied voltage.

The resistance-switching characteristics of memristive devices are closely related to the electrode and functional layer materials, that is, the same electrode when combined with different functional layer materials can present different resistance-switching behaviors and mechanisms. In other words, the same functional layer materials yield different resistance-switching behaviors with different electrodes. At present, researchers have realized the preparation of memristors based on a variety of materials, such as TiO_x,[7] ZnO,[8,9] VO_2,[10] TaO_x,[11] HfO_x,[12] and AlO_x.[13] The composition of metal oxides is simple, easy to prepare, and compatible with complementary metal oxide semiconductor (CMOS) devices.[14] In addition, there are solid electrolyte materials with lattice defects and rapid ion migration, such as Ag_2S,[15] SiO_2,[16–18] and Cu_2S.[19] Besides, organic materials with good flexibility and low cost, such as PVP,[20] PMMA,[21] and PFO,[22] have also been used to prepare memristive devices. Nowadays, the preparation of memristive devices can be achieved using many physical and chemical methods, such as atomic layer deposition, spin-coating method, magnetron sputtering, sol-gel method, pulsed laser deposition, and so on.[23–26]

In recent years, with the gradual improvement in the preparation and performance of memristors, the research focus has shifted from the preparation of devices to the development of artificial intelligence systems, neuromorphic devices and brain-like chips (Fig. 1d). Owing to the various excellent electrical properties of memristors, researchers have realized different applications, including memory circuits, logic operations, neural networks, nonlinear systems, and so on.[27–31] Pi *et al.* reported a 3 × 3 memristor array with the $Pt/TaO_x/HfO_2/Pt$ structure and feature size of 2 nm,[32] demonstrating extremely high scalability, which facilitates the implementation of storage and computing systems with low power consumption and high density. Besides, a diffusion dynamics-based memristor has been developed,[33] in which the dynamic process of Ag nanoparticles doped into the oxide dielectric layer is similar to the biodynamics of Ca^+ ions in chemical synapses, suggesting that this memristor is capable of naturally simulating bio-synaptic behaviors, such as short-time plasticity (STP), paired-pulse facilitation (PPF), long-term plasticity (LTP), and spike-timing-dependent plasticity (STDP). Based on the above synaptic properties, artificial nociceptors and artificial sensory alarm systems can be also constructed and designed using diffusion-type memristors, thus indicating the possibility of its application in bionic robots. Further, Wong's group constructed a neuromorphic vision system with low power consumption and high fault tolerance based on a stacked oxide synaptic device,[34] simulating the orientation detection function of the visual cortex of the human brain. Miao *et al.* researched the application of memristor-based logic operations[35] and have successfully designed the memristor arithmetic logic unit, logical operations, *n*-bit full adders, and various operation functions. Using this logic unit, a high-performance processor with reconfigurability, low power consumption, and small size was constructed. Besides, this device exhibited near-zero static power consumption due to its integrated memory-computing feature.

Therefore, memristor devices have great potential for application in neuromorphic systems, among which memristor-based

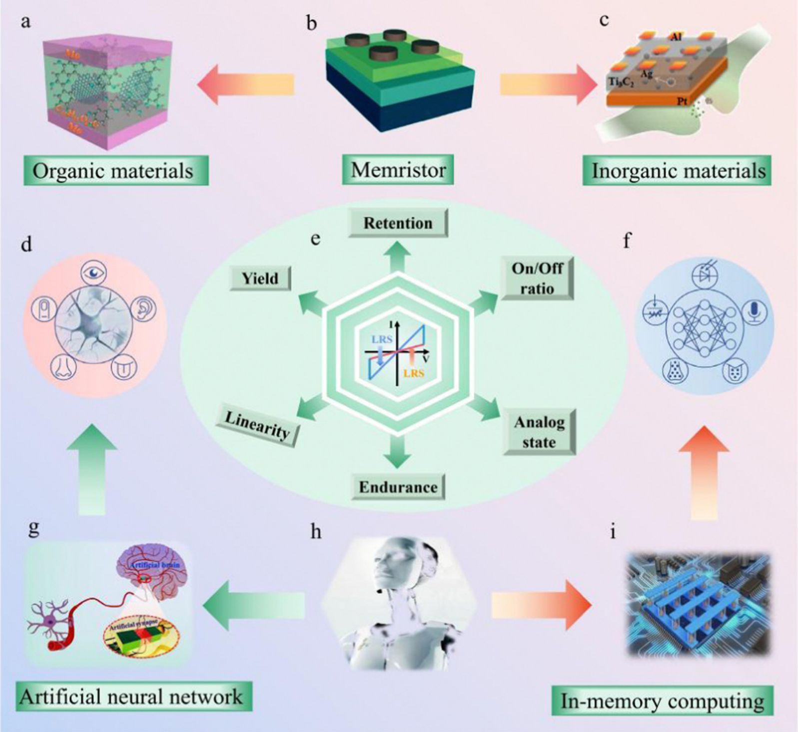

Fig. 2 Material classification and applications of memristors. (a) The schematic of organic materials. Panel a is reproduced with permission.[39] Copyright 2021, American Chemical Society. (b) The memristor structure. (c) The schematic of the inorganic material. Panel c is reproduced with permission.[37] Copyright 2021, Elsevier. (d) Brain neural networks and perception. Panel d is reproduced with permission.[24] Copyright 2022, Elsevier. (e) The metric parameters of a memristor. (f) An artificial multisensory neural network. Panel f is reproduced with permission.[24] Copyright 2022, Elsevier. (g) Artificial neural network and artificial synapses. Panel g is reproduced with permission.[39] Copyright 2021, American Chemical Society. (h) An artificial intelligence robot. (i) Schematic diagram of In-memory computing.

neural network is one of the focus areas in current research.[36–38] The advantages of memristors in the simulation of synapses and neural networks make them one of the most ideal devices used in neuromorphic computing for artificial intelligence applications. In this paper, memristors fabricated from different materials are reviewed for basic performance characteristics, the connection with neural networks, and their application in artificial intelligence. Furthermore, the current challenges are summarized and some strategies are proposed. The schematic in Fig. 2 presents an overview of this review.

1.2 Memristor-based neural networks

The successful preparation of artificial brain-like chips has always been considered the basis for the development of supercomputers because the human brain is the best-known computing system with superb parallel computing capability. It is generally believed that the main computational unit of the human brain is the neuron, which receives external input signals through dendrites and transmits signals to other neurons *via* connections called synapses. A key feature of the biosynapse is that it can scale the signals that pass through, and the scale factor is called weight. The learning behavior of the human brain is considered to be based on the process of changing the relevant synapse weight.[36,40] At present, the artificial neural network is considered the core algorithm of artificial intelligence represented by deep learning. Neural networks can perform a weighted summation of all input signals in the process of calculation. The deep hierarchical nonlinear processing of neural networks enables automatic and efficient learning of senior abstract representations in higher dimensional data, which has revolutionized the multimedia fields, such as images and videos,[41] speech and language.[42] It also plays an increasingly important role in the emerging fields of medical health and robotics.[43–45] With continuous performance improvement, neural networks are increasingly deployed in some practical industrial applications, including manufacturing, asset management, mobile phone voice assistance, autonomous driving, and so on. Therefore, using memristors to simulate synapses is considered one of the key steps to building artificial neural networks.

Nowadays, although artificial neural networks have been proposed to solve the von Neumann bottleneck,[46,47] the algorithm of artificial neural networks is still based on traditional computers, which leads to a series of problems, such as limited computing power and low energy efficiency. With the advent of artificial intelligence, the internet of things and machine learning, the demand for computing power has increased exponentially. For example, for the AlphaGo implemented using 1200 central processing units (CPUs) and 180 image processors (GPUs), the power consumption is as high as hundreds of thousands of Watts.[48] During the learning phase, most of the energy consumption is dedicated to the programming operations of the memory and the reading operations of the synaptic devices. Therefore, energy per operation is a key factor for estimating the energy efficiency of neuron-inspired computing chips. A neural network system composed of $\sim 10^{11}$ neurons and 10^{15} synapses can process a large amount of information with very low power consumption (20 W), and the operation consumption per stimulus is only 1–100 fJ.[47,49] Nowadays, most resistive random access memory (RRAM) devices show programming energy of around 100 fJ–10 pJ, while most phase change memory (PCM) devices have higher programming energy of 10–100 pJ. On the other hand, because the memristive device has a very high stack density (<2 nm), and the switching speed can be very fast (<0.1 ns),[32,50] it only needs a small amount of energy and can be manufactured in a smaller size. However, the complex manufacturing process and high energy consumption bring huge difficulties to large-scale integrated circuits. The schematic of a memristor in which the functional layer can be made of inorganic and organic materials is shown in Fig. 1d, and the memristor can serve as the core hardware for both brain-like chips and artificial intelligence algorithms. In order to effectively implement neural network algorithms, more promising hardware needs to be developed, and memristors are expected to be a central component of the new hardware. The memristor has great advantages compared with traditional devices used in the construction of neural networks. The resistive switching behavior of memristors can be divided into two types according to the resistive changes: analog type and digital type. Among them, the resistive state of the analog-type memristor is continuous, and its conductance can be gradually changed *via* electrical pulses, which can be used to simulate the continuous change in bio-synaptic weights and bio-neuronal membrane potential under external stimulation.[51] However, the resistance states of the digital type memristor are discrete during the scanning of the voltage and can be converted between the HRS and LRS, thus achieving sudden binary conductance states for simulating all or no characteristics of the neuron network. Different memristors can also exhibit abhorrent retention characteristics, that is, the slow change in electrical conductivity in the device is similar to the process of enhancing and inhibiting the connection strength of bio-synapses. In addition, being a type of two-terminal device, the memristor has a similar structure to the neural synapse. The size of the memristor can be reduced to the nanometer level, and the integrated array density can even reach the density of the bio-synapses in the brain, which gives the memristor a distinct advantage in neural network construction. In terms of transmission mechanisms, the synapse is typically composed of a presynaptic neuron, a postsynaptic neuron, and a synaptic gap. The synapse enables signaling and behavioral changes through the transmission of Ca^{2+} ions and K^+ ions. The top electrode, bottom electrode and functional layer of the memristive device correspond to the bio-synaptic structure.[52] Interestingly, the memristor can also regulate conductance by varying the migration of ions in the functional layer. At present, in most memristors, the change in electrical conductivity is the result of ion movements, such as the migration of metal ions, oxygen vacancies and carriers captured at the interface. Therefore, the memristor is capable of acting as an electronic synapse and can be further applied in the construction of artificial neural networks.[53] With the development in recent years, it has been found that memristors can achieve a variety of synaptic functions, especially in learning and memory. Nevertheless, memristors still have some challenges in realizing the perfect bio-synaptic simulation. The fundamental challenge is that it is much more difficult (thus paying more energy) to move the ions/defects in solid-state devices than the movement of Ca^+ ions in a liquid environment as in bio-synapses. Fig. 3 shows the principle of a memristor

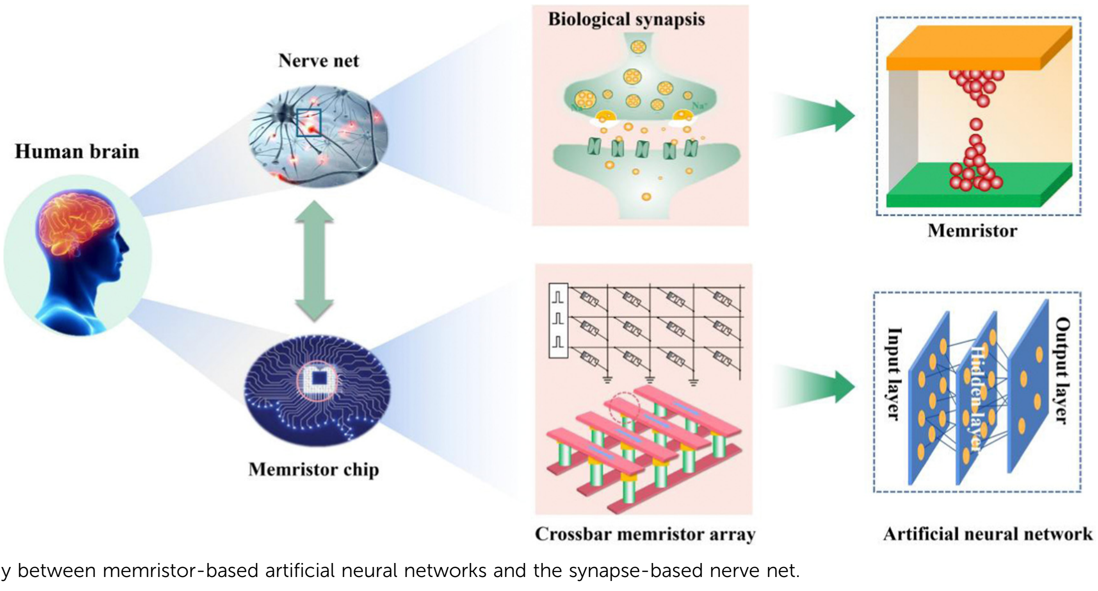

Fig. 3 Analogy between memristor-based artificial neural networks and the synapse-based nerve net.

used to simulate a bio-synapse and its analogy with the bio-synapse.

In the neuromorphic hardware system, neural networks are divided into artificial neural networks (ANN) and spike neural networks (SNN). ANN can be extended to deep neural networks (DNN) and convolutional neural networks (CNN). In SNNs, artificial synapses are used to simulate STDP for unsupervised learning.[54] To apply DNNs to achieve high recognition accuracy, it is necessary to develop artificial synapses with ideal synaptic characteristics. The synaptic characteristics of artificial synapses, such as dynamic range, multi-level states, nonlinearity, cycle-to-cycle variation, and device-to-device variation in weight update, will affect DNN accuracy.[47] In general, brain-inspired neural network synapses require memristors with a wide dynamic range to accommodate a large number of resistive states. Low fluctuation, low drift and high absolute resistance value are required for precision computing while high endurance is needed during training/programming.[53] In SNNs, artificial synapses are used to simulate STDP for unsupervised learning, which cannot guarantee high performance in general learning tasks.[54,55] Therefore, SNNs are more suitable for low-precision computing applications. SNNs are mostly bio-plausible, real-time, less power-consuming, and suitable for brain-inspired computing systems. Hence, the synaptic plasticity of memristors is required in SNNs. ANNs have fast computing speed and high computing intensity, so they are suitable for the von Neumann computing system. For ANNs with a few layers (one or two layers), analog conductance with a wide dynamic range and high retention is an indispensable factor. Furthermore, effective neural network training also requires lower device variation and symmetrical weight update. For DNNs and CNNs, the synaptic weight is adjusted during training. In this process, increasing the number of data states can improve the learning ability and accuracy of the neural network. The weight update feature will be linear and symmetrical in order to change the synaptic weight to the desired value during training. Therefore, long retention, low power, good scalability and large dynamic range are also required characteristics of the device in addition to analog conductance.[56]

1.2.1 Artificial neural network. The ANN is a computational model in the field of artificial intelligence and is inspired by the bio-neural network; its organizational structure is similar to the neural connections in the brain, as shown in Fig. 4a. The artificial neurons are connected through artificial synapses, and the neural signals are transmitted from one neuron to other neurons. In this process, the synaptic signals are collected, integrated, converted, and passed to the nervous system by artificial neurons. ANNs can simulate the functions of bio-neural networks, such as associative memory, conditioned reflexes, and visual recognition. Besides, from the data, the ANN can learn specific tasks directly without programming by humans and also has some generalization ability, so the ANN can make judgments based on what it learns from its invisible surroundings. For example, through training with large amounts of data, ANN has been shown to learn and recognize objects,[57–60] which is the biggest difference from traditional machine learning. Structurally, neural networks are usually organized into a hierarchical structure, which mainly includes an input layer, a hidden layer and an output layer, of which the hidden layer can be constructed as a multilayer structure.[61–64] The neurons in the input layer can receive external input to perform a nonlinear transformation on the weighted sum and provide an output to the hidden layer. The information in the hidden layer is transmitted to the output layer, which finally displays the result to the user. Actually, modern neural network models have more abundant structures and more diversified hidden layer choices.[65–67]

The neural network has two working mechanisms: one is the inference process, and the other is the learning process, which is also known as the training process. A loss function is generally constructed to characterize the convergence degree of the model during the training process. In each hidden layer, the error derivative of each output unit is first calculated, which is the weighted sum of the error derivatives of the total input for

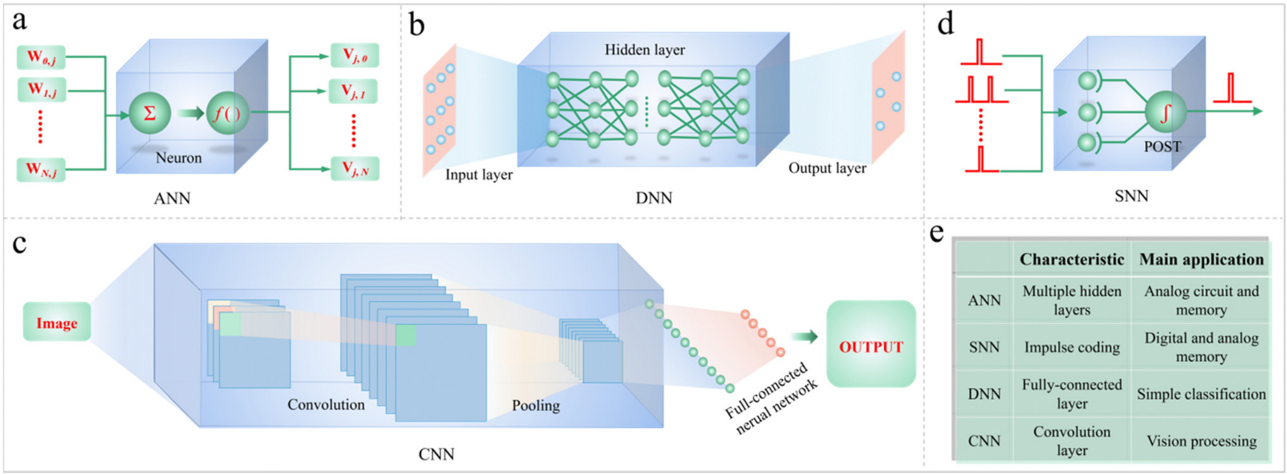

	Characteristic	Main application
ANN	Multiple hidden layers	Analog circuit and memory
SNN	Impulse coding	Digital and analog memory
DNN	Fully-connected layer	Simple classification
CNN	Convolution layer	Vision processing

Fig. 4 The backbone architectures of various neural networks. (a) ANN; (b) DNN; (c) CNN; (d) SNN. (e) The comparison of characteristics and main applications between ANN, DNN, CNN and SNN.

the unit in the previous layer. Then, the output error derivative is multiplied by the gradient of the activation function $f(z)$, thereby converting the output error derivative into the input error derivative.[68–70] In the output layer, the derivative of the unit output error is calculated by a differential loss function. During the training process, the training algorithm is generally combined with some optimization algorithms to make the network weights converge to an optimal solution. In the inference process, the total input z of each neuron is calculated in each layer, and this total input is the weighted sum of all the outputs from every neuron in the front layer. Then, the total input z is used as the output of the neurons in this layer after being acted upon *via* the nonlinear function f. The output of each neuron layer is used as the input of the neurons in the next layer, and the final output is transmitted to the output layer. In the training process, the model first performs the forward inference process to output the decision, and then back-propagates the error and updates the weights of the model accordingly.[71,72] The weights of the model are invariant during this process. Therefore, the neural network must perform a large number of matrix-vector product operations during inference and training, placing huge computational power demands on the hardware.

1.2.2 Deep neural network. The DNN is a kind of artificial neural network with multilayer neurons, also known as deep learning, as shown in Fig. 4b, which is a branch of machine learning.[73] The predecessor of DNN is the perceptron, the simplest of which contains only one neuron. DNN usually adopts a relatively simple neuron model, in which the neurons do not depend on time during operation, and the neural signals are propagated between the input and output layers in the numerical form. Layering is another feature of DNN, wherein neurons in the same layer are not connected to each other, while neurons in different layers are connected together through synapses.[74,75] Generally, DNNs are divided into the feed-forward type and cyclic type. The topology of a cyclic network contains directed loops, in which the data flow in the feed-forward network is unidirectional, and the data moves along the network layers. A DNN is obtained by connecting many layers of such neural networks. The neurons in layer i collect the neural signals from the front layer and send these signals to the next layer $i + 1$ through integration processing. If every neuron in layer i is linked to a neuron in the front layer, it is called a fully-connected neural network or multilayer perceptron.[76] The main feature of DNNs is the presence of a large number of layers. Current residual neural networks have up to 152 layers, and each layer in the DNN converts its input into a more abstract representation. Compared to neural networks with fewer layers, DNNs perform complex nonlinear mapping of input samples to extract more abstract concepts, which is vital to the implementation of artificial intelligence.

1.2.3 Convolutional neural network. As a further development of ANN and DNN, CNN has been employed in other aspects, such as image processing and image recognition. CNN is a type of feedforward neural network with a deep structure and convolutional processing, which is one of the typical algorithms of deep learning, as shown in Fig. 4c. CNNs have the ability to represent learning and can classify the input data according to their hierarchical structure. In 1998, Lecun *et al.* proposed a convolutional model to improve the connectivity and reuse of neural networks.[77] However, due to the lack of computing power at that time, the online training problem was still difficult to solve. In the following ten years, the research on CNN basically stagnated. It was not until 2012 that CNN represented by AlexNet really began to attract the attention of researchers. A CNN is usually composed of a convolution layer, activation layer, normalization layer, pooling layer and full connection layer. As a typical model in the field of deep learning, CNNs play an irreplaceable role in computer-based vision applications. CNNs can automatically extract features during image processing and implicitly learn from the data so as to effectively mine the high-level semantic features of the image without relying on manual feature extraction. The training process of CNNs mainly includes forward propagation and back propagation stages. In the forward propagation process, the features of the original data are gradually represented and learned through these superimposed different modules, and finally passed to the target. In the back propagation stage, the objective function is employed to measure the deviation between the actual value of the output and the corresponding predicted value, and the weights and deviations are updated. CNNs have been developed rapidly, achieving unprecedented accuracy in target classification and recognition based on computer vision,[77–80] object detection,[81] and scene analysis.[82] This has successfully solved some issues in multiple research directions, including image classification, image semantic segmentation, video tracking, and speech analysis. Nowadays, reducing latency, lowering power consumption and saving energy are the main challenges in deploying CNNs in embedded terminals.

1.2.4 Spiking neural network. The SNN adds randomness to the network neurons, as shown in Fig. 4d, and requires advanced statistical methods and efficient training algorithms. In addition, the SNN is more similar to bio-neural networks, and its model is more complex and variable, which greatly increases the difficulty of applying random neural networks in artificial intelligence. Currently, SNN has been mainly used in neuroscience research as it transmits information through discrete spike trains, and the information is further encoded in time series. In an SNN, neurons continuously output signals, and both neurons and synapses contain internal states. Generally, the state change inside the neuron is represented by a differential equation. The impulses input to the neurons can make the membrane potential rise or fall, thereby simulating the excitation and inhibition of synapses. Different from the DNN, the information encoding of SNN is diverse, mainly including pulse frequency encoding, pulse interval encoding and pulse amplitude encoding. Model training is one of the core problems of SNN, wherein unsupervised learning is the ultimate goal of neural network learning. In the process of unsupervised learning, the pulse sequence is first input into the SNN, and then the weight matrix in the neural network is adjusted so that the pulses generated *via* the SNN gradually approach the corresponding target pulses, thereby achieving the purpose of machine learning. The SNN can also accomplish the simulation of analog and digital circuits. In the process of analog circuit implementation, the SNN can directly simulate the dynamics of the brain, which is beneficial to obtain a better response time, and then integrate with more neurons and synapses. During digital circuit implementation, the SNN can be reprogrammed and reconfigured online to further achieve high accuracy and strong noise immunity. The SNN has many internal variables and complex connections; thus it needs to consume more computing resources and energy than the DNN under traditional architectures. Nowadays, *in situ* computing and synaptic learning are employed as effective approaches to solve the large computation-intensive and many internal states. In particular, the crossbar array of memristors can realize synaptic training, and its crossbar structure can provide sufficient interconnectivity. A comparison of the characteristics and main applications of ANN, SNN, DNN and CNN is shown in Fig. 4e.

1.3 The development of memristor-based neural networks

The memristor-based neural networks under different information coding mainly include ANNs and SNNs. Among them, the ANN pursues higher computational efficiency in data-intensive tasks, while SNN provides excellent power efficiency by simulating biological neural networks with peak-time encoded neuron values. In the aspect of algorithm training, *ex situ* and *in situ* training are the two main training methods used in the neuromorphic simulation. In the *ex situ* method, the data are trained in the software system, and then, the calculated weights are loaded into the analog memristor array, demanding higher requirements of retention, bit yield, and uniformity. In contrast, a neuromorphic computing system with *in situ* training can update the weights on the chip, and thus, it has better immunity to retention degradation, state-stuck issues, and variations than *ex situ* training. On the hardware side, the basic operations of the classical ANN hardware are limited to multiplication, addition, and activation, which can be performed even by CMOS circuits (such as GPU). However, for neural networks with a large number of computational parameters, although the CMOS circuit is scalable, it still cannot match the neuromorphic simulation of the ANN. At present, many topology-learning algorithms have been developed based on ANN software and hardware. In 2018, high-precision analog tuning and control of a memristor with 128 × 64 1M-1T Ta/HfO_2 array were demonstrated.[83] The memristor-based system exhibited an image recognition accuracy of 89.9% for the MNIST digit set. In 2019, a WO_{3-x}-based memristor with coexisting analog and digital resistance switches was realized, and a new analog-digital hybrid ANN memristor was further developed.[84] This device demonstrated adjustable learning accuracy and speed in pattern recognition and simulates STDP learning. In 2020, a memristor crossbar was used for full hardware implementation.[85] A five-layer CNN was constructed by integrating 2048 memristor array units to realize MNIST[10] image recognition, and a high precision of more than 96% was achieved. In addition, this memristor array demonstrated the replication and parallel processing of multiple identical kernels, which was more than two orders of magnitude more efficient than the most advanced graphics processing units of the time, and could be scaled up to larger networks. In 2021, Wang *et al.* integrated photosensing, storage, and *in situ* computing into the memristor array, greatly improving the integration of hardware and the efficiency of the chip.[86] The accuracy of the photoelectric memristor in neuromorphic computing was up to 86.7% *via* recognizing the facial images of different people. In addition, the integrated memristor demonstrated the attractive biomimetic sensor-in-sensor computing behavior of the photoelectric memristor, providing a possibility for the application of the photoelectric memristor in the next generation of reconfigurable sensor-memory-computing integrated paradigm. Recently, a new system inspired by neural modulation in the brain has been proposed, in which the trained synapses are temporarily hidden during the training of the spiking neural networks and then merged for inferencing.[87] The self-recirculating and non-electrostatic memristor unit was integrated onto 32 × 32 medium-density polyethylene for hardware demonstration. The energy consumption of the memristor array was reduced by 37% for unsupervised learning of the MNIST dataset, which can be used in spiking neural networks for efficient learning.

The third-generation SNN, which is inspired by the animal brain, enables the simulation of the desirable properties of compact biological neurons and presents significantly improved cognitive and computational performance. The most striking feature of the SNN is that it incorporates the concept of time into operations with discrete values. Many attempts have been made to implement STDP in artificial synaptic chips because the temporal and spatial variables are crucial for computing information in SNNs. Li *et al.* simulated 128 × 64 vector matrix multiplication using a reconfigurable HfO-based memristor crossbar switching, whose array size was up to 128 × 64 units.[88] This 1T-1R memristor demonstrated high-precision image compression and convolutional filtering. In 2021, a novel CuS/GeSe memristor was proposed to realize electron-randomized neurons according to the randomness in biological ion channels.[89] Compared with the SNN based on deterministic neurons, this SNN system could estimate the uncertainty in prediction and the fidelity of judgment greatly improved by 81.2%. Recently, a HfO_2-based OxRAM memristor was stacked on a Ge–Se–Sb–N-based ovonic threshold switch (OTS) back-end selector for the implementation of high-density binarized SNN synaptic weight hardware.[90] This memristor-based system was optimized for 1S1R low-reading bit error rate in high-frequency reasoning. For the MNIST handwritten digit recognition task, a general guide was given to reduce the system footprint and power consumption for maximizing the inference frequency and accuracy.

2. Research progress

2.1 Inorganic memristor-based neural networks

2.1.1 2D-MXenes. Two-dimensional (2D) material-based memristors have attracted extensive attention in synaptic simulation due to their low-dimensional structures and unique physical and chemical properties. Memristive devices based on 2D materials have distinctive and superior device properties, including large RS ratios,[91] low switching voltages,[92,93] small device variations,[94] and the ability to switch between thresholds and bipolars.[95] In addition, 2D materials have near-atomic thickness and high-density crossbar arrays, which endow them with great potential in manufacturing ultra-thin memory synapses with high-density integration and high operational reliability. The plasticity of bio-synapses can be effectively modeled using the analog-resistive switching behavior of 2D material-based memristors.[96,97]

MXene is a novel 2D transition metal carbonitride belonging to the carbide and nitride family, and has become a promising 2D material in the fields of energy conversion and storage due to its interesting physical and chemical properties.[98] As an emerging member of the 2D material family, the MXene Ti_3C_2 has received extensive attention due to its excellent memristive properties and miniature size. Wang *et al.* improved the electronic properties of 2D-MXene Ti_3C_2-based memristors *via* doping Ag nanoparticles into the functional layer,[37] and the structure of the as-prepared memristor is shown in Fig. 5a. Compared with pure Ti_3C_2-based memristive devices, the Ag-nanoparticle-doped device exhibited bidirectional continuous current-transition behavior. Fig. 5b shows that the peak energy consumption of the Al/Ti_3C_2:Ag/Pt device was as low as 0.35 pJ, which enables the unique simulation of synaptic behaviours, including short-term memory (STM) and long-term memory (LTM) characteristics, as shown in Fig. 5c. In addition, several decimal arithmetic operations were demonstrated in the Al/Ti_3C_2:Ag/Pt memristor (Fig. 5d). Further, Zhang *et al.* demonstrated a hybrid ferroelectric Cu/MXene/PZT memristor, in which the 2D MXene material Ti_3C_2 intercalated into conventional PZT to improve the performance of the ferroelectric memristor.[99] In contrast, the Cu/Ti_3C_2/PZT/Pt-based ferroelectric memristor exhibited superior characteristics, such as lower switching voltage, reproducible RS behavior, lower power dissipation and a higher on/off ratio of up to 10^6,[99] as shown in Fig. 5e. In addition to simulating bio-synapses, the device also demonstrated the PPF and STDP functions, as illustrated in Fig. 5f. In particular, the learning and recognition accuracy for images was as high as 95.13% (Fig. 5g). Sokolov *et al.* applied MXene ($Ti_3C_2T_x$) sheets to electronic synapses based on their unique insulating properties,[100] which led to the threshold-shift switching properties because of Ag^+ ions migration kinetics. Using Ag^+ ions migration, the kinetic behaviour of Ca^{2+} ions in the bio-synapses can be simulated. The bio-synaptic functions, including PPF, strong electric post-enhancement (PTP), STP and LTP, were further realized, as shown in Fig. 5h.

In addition to Ti_3C_2, other MXenes have also been used in the construction of memristor-based artificial neural networks. In 2021, Wang *et al.* designed and constructed a multimodal MXene-ZnO memristive device that combined visual sensing, relative humidity sensing and preprocessing to simulate the unique visual behavior of the human eyes,[101] as shown in Fig. 6a. The resistive switching behavior of the multi-field-controlled MXene-ZnO-based memristor depended on the formation of oxygen vacancy filaments *via* photon or proton tuning. The data collected from a single device over 100 scanning cycles and the predicted statistical distribution of the resistance ratio are shown in Fig. 6b. The time variability of the on/off ratio in the positive scan and the negative scan was 0.396 and 0.452, respectively. Fig. 6c provides the corresponding current values of the memristive device at different bending angles. The reading currents in the two conductance states were stable in the cycle of four different curvatures, proving the feasibility of its application as a flexible sensing memristor. The MXene-ZnO-based memristor with an in-sensor computational function can be used both as a sensor for information preprocessing and a synapse for the weight-updating process under environments with different humidity. To exploit the high-efficiency neuromorphic hardware networks, a multifunctional neuromorphic device based on 2D-MXenes has recently been proposed.[102] This device can be programmed to achieve synaptic or neuronal functions, thus breaking the boundaries between neurons and synaptic modules and enabling efficient neuromorphic networks. The structure of the memristive device with the Ag/2D-MXene ($Ti_3C_2T_x$)-doped polyvinyl alcohol (PVA)/indium tin oxide (ITO) structure is shown in Fig. 6d. A neural network composed of multiple neuron-synaptic transistors was designed for authenticity data recognition. The hardware sources of the neuromorphic device could be uniformly redistributed, and the topology structure of the memristor array could be adjusted. This design increased the computing speed and reduced the number of devices. Fig. 6e depicts the implementation of the artificial synaptic simulation based on the as-prepared memristor. Based on this design, a hardware system was developed with a recognition accuracy of about 80%, which can be applied for face recognition (Fig. 6f).

2.1.2 Traditional oxide materials. Oxide-based memristive devices have been widely accepted as one of the most prospective technologies for next-generation nonvolatile memory and neuromorphic computing. Usually, the generation of conductive filaments determines the switching process of memristors. However, conductive filaments are not easy to control and lead to large device-to-device variations among memristive devices, further hindering the growth of unified performance memristors. To address this situation, Wan *et al.* demonstrated an oxide memristive device with a spontaneous phase-separation process,[103] in which it is enabled to form an amorphous TiO_2 switching dielectric that is distributed among crystalline CoO grains. Cycle tests over more than 1000 continuous switching cycles showed the stable resistive switching behavior of the memristor, as shown in Fig. 7a. The as-designed material structure also promoted the formation and rupture of conductive filaments during the switching process, enabling chemical switching and low switching power. Recently, a study has revealed the signal simulation behavior of a TiO_2-based memristor in neuromorphic computing.[104] In this work, the Ag/TiO_2/Pt memristor was fabricated using pulsed laser deposition, resulting in excellent digital and analog switching behavior with a memory window of about $\sim 10^3$. This memristor could provide multiple conductance

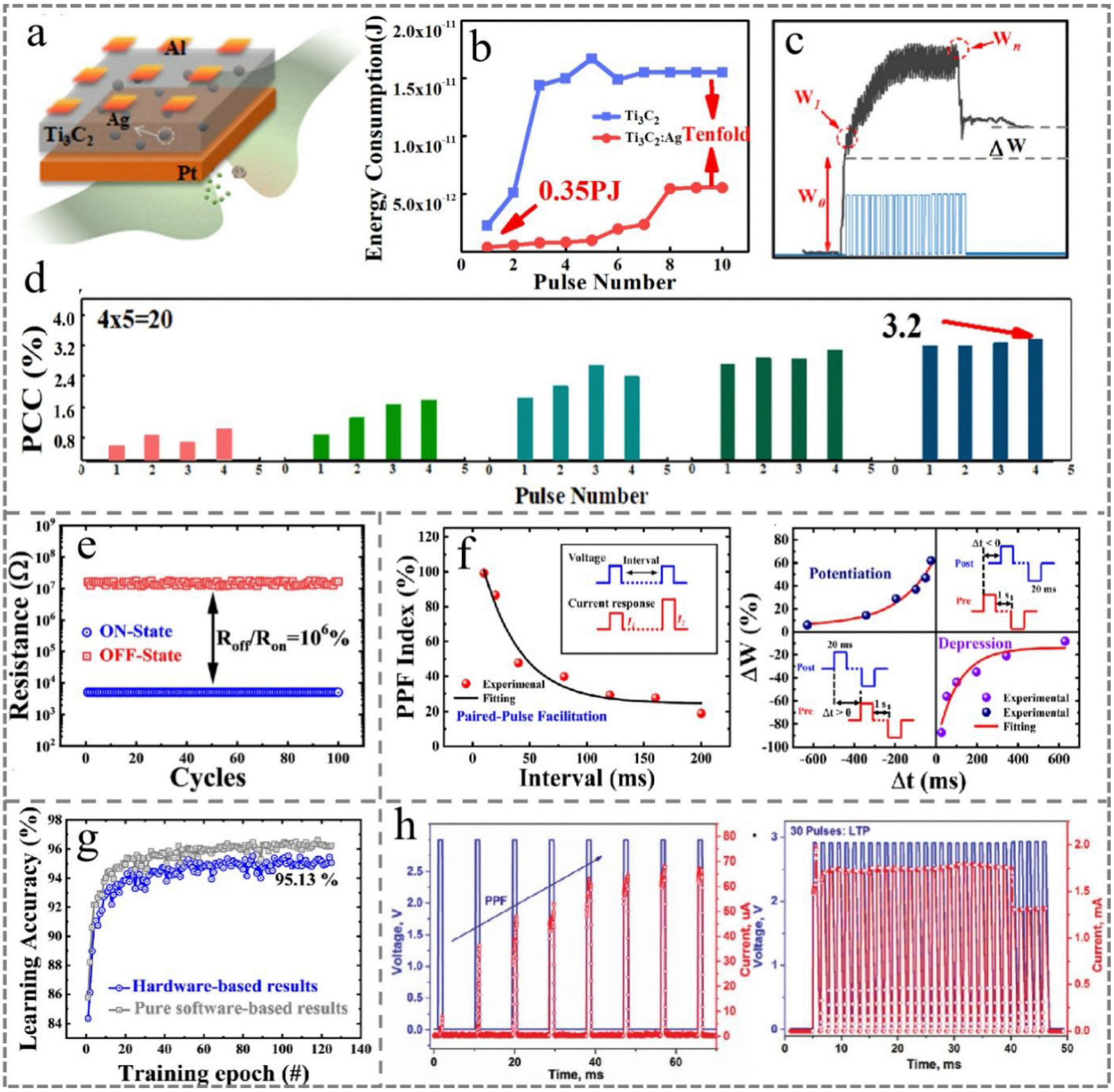

Fig. 5 (a) The structure of the Al/Ti_3C_2:Ag/Pt memristor. (b) The energy consumption variation in Ti_3C_2- and Ti_3C_2:Ag-based memristive devices. (c) The implementation of memory properties and the modification of w_n/w_l with various pulse durations for STM and LTM. (d) The demonstration of commutative multiplication arithmetic on the Al/Ti_3C_2:Ag/Pt memristive device. Panels (a–d) are reproduced with permission.[37] Copyright 2020, Elsevier. (e) The endurance test of the Cu/Ti_3C_2/PZT/Pt memristor shows the on/off ratio for 100 cycles. (f) The simulation of the typical PPF (left) and STDP (right) behaviors of the bio-synapse; the insets display the pulse protocols. (g) The neural network learning accuracy of the MXene-PZT-based memristor. Panels (e–g) are reproduced with permission.[99] Copyright 2022, Elsevier. (h) Experimentally emulated PPF phenomenon (left) and artificial synaptic memory properties during the STP-to-LTP transition of the MXene-based memristive device (right). Panel h is reproduced with permission.[100] Copyright 2021, Elsevier.

levels and successfully realize the basic synaptic function. The neural network simulation of the pattern recognition task was carried out using the MNIST data set, and the recognition accuracy was as high as 95.98%. Besides, a memristor with the Pt/$LiCoO_2$/SiO_2/Si structure was prepared,[105] as shown in Fig. 7b. This biomimetic structure exhibited a high on/off ratio above 10^8 and a long retention time of about 10^5 s even at a small read voltage of 0.5 V (Fig. 7c). At the same time, this memristive device realized typical synaptic functions, such as STDP and nonlinear transmission, as shown in Fig. 7d. In addition, other binary metal oxide-based memristive devices have also exhibited better resistive-switching memory properties. For instance, in 2021, Parit *et al.* combined the threshold-switching characteristics of NbO and the memory-switching characteristics of TaO in one device, proposing a TiN/NbO/TiN/TaO/TiN-based memristive device.[106] The experimental results indicate that the self-selective NbO–TaO-based memristor showed excellent performance in the nonvolatile RRAM application, including a high

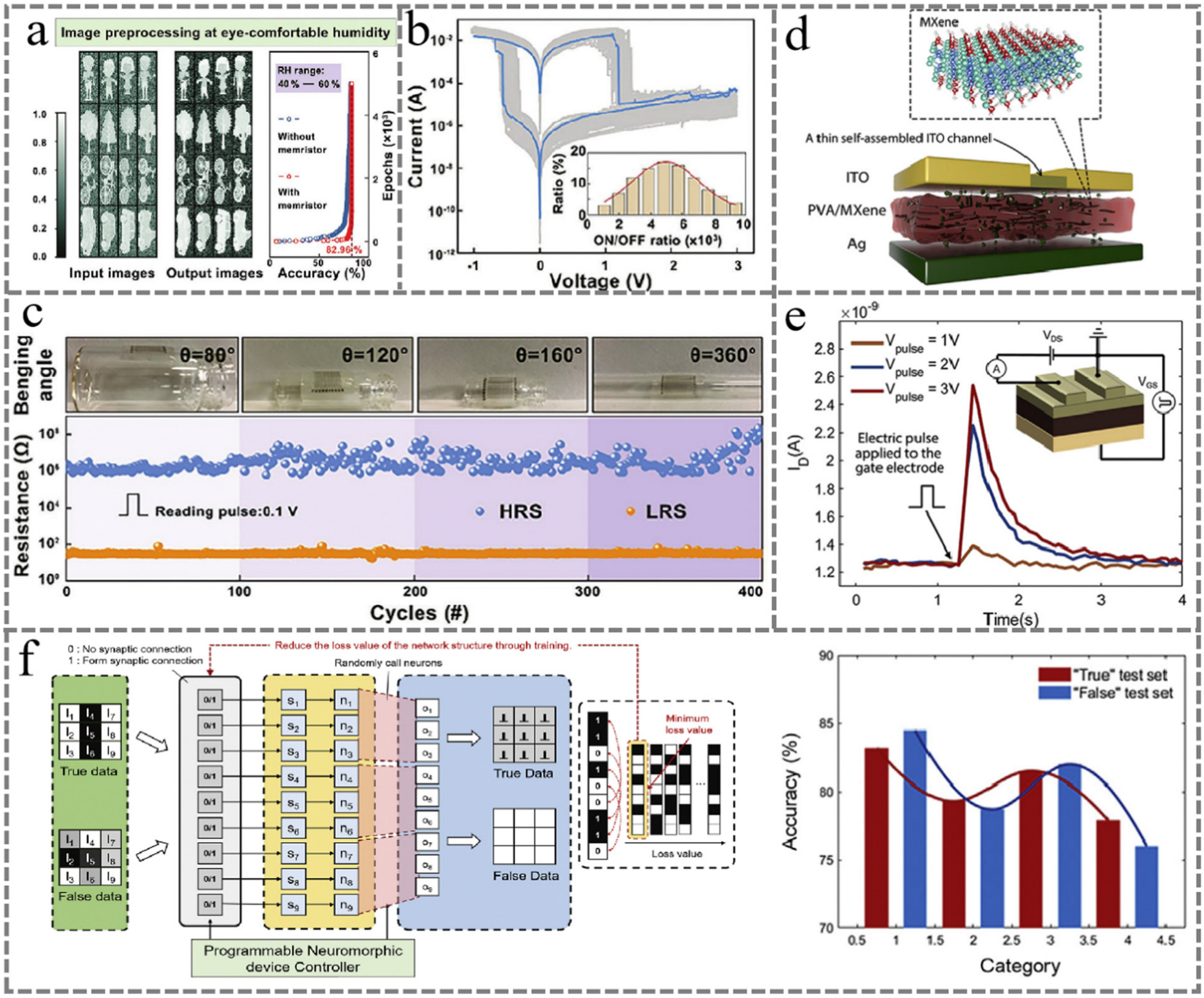

Fig. 6 (a) The output image of the simulated artificial retinal sensing system and its image recognition rate after preprocessing (right). (b) The resistive-switching characteristics of the memristive device with the statistical switching ratio distribution. (c) The on/off current in the LRS and HRS at a read voltage of +0.1 V. The upper panel exhibits the optical images of the memristors at different bending angles. Panels (a–c) are reproduced with permission.[101] Copyright 2021, Wiley-VCH. (d) Schematic of the switchable neuronal-synaptic transistor and the molecular structure of MXene. (e) The excitatory post-synaptic current triggered by the pre-synaptic pulse as a function of time. (f) The structure of the hardware networks with the neuromorphic (left) and image-recognition accuracy of the switchable neuronal-synaptic transistor system (right). Panels (d–f) are reproduced with permission.[102] Copyright 2022, Elsevier.

read window (32.6), a high nonlinearity of ~141 and a low OFF current of ~1.22 μA (Fig. 7e).

In addition to binary metal oxides, the memristor and artificial synaptic device using perovskites as the active layer have also been applied in neuromorphic computing in recent years. Zeng *et al.* fabricated a memristor with an Ag/$Cs_3Cu_2I_5$/ITO structure using uniform $Cs_3Cu_2I_5$ perovskite films as the functional layer in the device.[107] Fig. 8a exhibits the structure of the as-prepared Ag/$Cs_3Cu_2I_5$/ITO memristor. Fig. 8b depicts the repeatable *I–V* characteristics of the optimized memristor over 50 sweeps without collapse, and an on/off ratio above 10^2 was recorded over 100 consecutive cycles at a read voltage of 0.1 V, as shown in Fig. 8c. In addition, the obtained nonvolatile memristor exhibited bipolar resistive-switching behavior with a long retention time ($>10^4$ s), a low operating voltage ($<\pm1$ V) and stable endurance (>100 cycles). In 2021, John *et al.* demonstrated a pyridine-based halide perovskite material with a one-dimensional (1D) single molecular lead iodide lattice, namely prosylpyridine lead iodide, which was designed for password generation and device authentication.[108] The memristor with the Ag/PMMA/PrPyr[PbI_3]/PEDOT:PSS/ITO structure showed excellent bipolar resistive-switching behavior with a high switching ratio of about 10^5. The crystal structure of PrPyr[PbI_3] and the SEM image of the memristive device can be seen in Fig. 8d, and the durability test in the changing current mode showed excellent stability (Fig. 8e). Besides, this memristive device could sustain a high on/off ratio of above 10^5 over 450 switching cycles with a retention time of ~10^4 s (Fig. 8f).

2.1.3 Transition metal sulfides.

As another major member of the 2D material family, transition metal chalcogenides (TMCs) and their heterostructures are attractive candidates

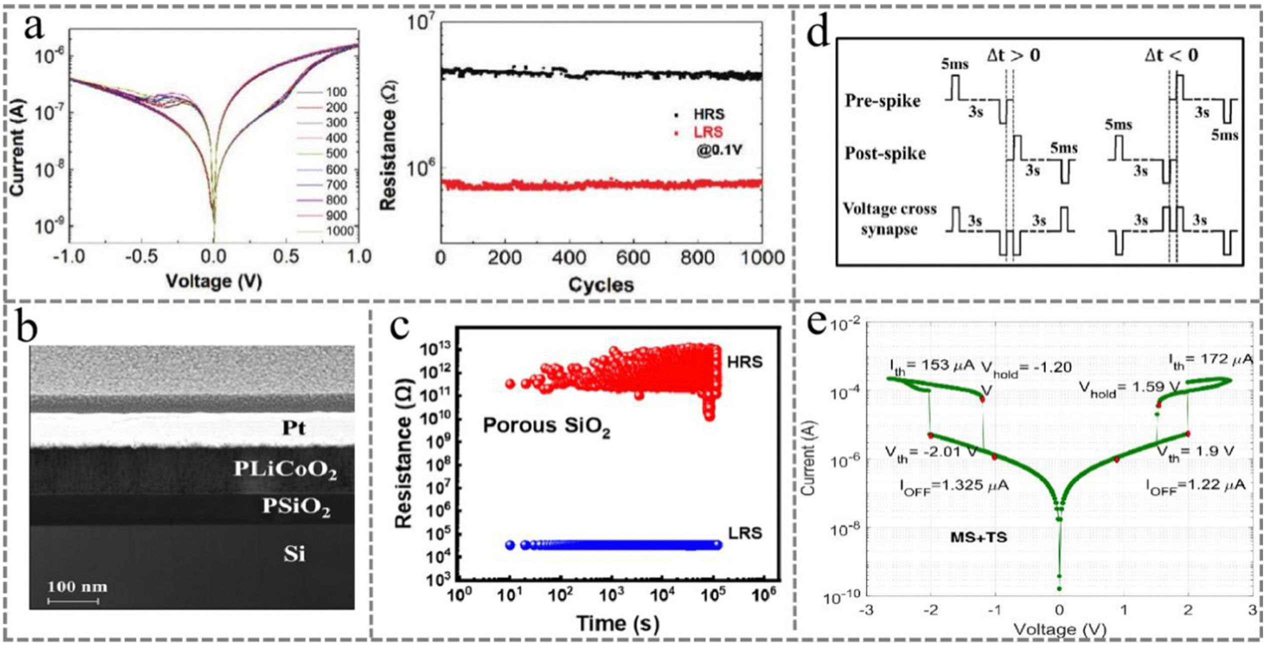

Fig. 7 (a) The *I*–*V* curves and resistance test of HRS and LRS per 100 cycles over 1000 switching cycles. Panel a is reproduced with permission.[103] Copyright 2020, Wiley-VCH. (b) A memristor with the Pt/$LiCoO_2$/SiO_2/Si structure. (c) The stability of the memristive device with the Pt/$LiCoO_2$/SiO_2/Si structure. (d) The STDP characteristics of the $PSiO_2$/$PLiCoO_2$ memristor. Panels (b–d) are reproduced with permission.[105] Copyright 2021, Nature Publishing Group. (e) The *I*–*V* characteristics (threshold switching + memory switching) at a voltage sweep speed of 1.77 V ms^{-1}. Panel e is reproduced with permission.[106] Copyright 2021, Elsevier.

for many electronic and optoelectronic devices, especially the synaptic device-based brain-inspired neuromorphic computing systems. Their unique characteristics, such as high endurance, clean surface, electrical and optical adjustability, and flexibility, make them suitable for manufacturing memristive devices with higher integration density, low power consumption and high scalability. Copper sulfide compounds have unique crystal structures, high electrical conductivity and earth ample sources and are considered one of the most promising materials for next-generation electronic devices. In 2019, Xu *et al.* reported a vertical memristive device, in which two MoS_2 monolayers were used as the functional layer of the device, and Cu and Ag were used as the top and bottom electrodes, respectively,[109] as shown in Fig. 9a. It was found that the Cu^{2+} ions were diffused by the MoS_2 molecular layers to form atomic-scale conductive filaments. This device had a near-atomic-layer thickness, and the switching voltage could be reduced to 0.1–0.2 V by electrochemical metallization. At the same time, consistent bipolar and analog switching behaviors were also achieved (Fig. 9b), thereby exhibiting synaptic-like learning behavior, such as STDP, as shown in Fig. 9c. Such a low switching voltage is not only suitable for low-power neuromorphic computing but also opens up the possibility of directly interfacing with mammalian neural networks in terms of voltage ranges close to biological action potentials. In 2022, Yin *et al.* successfully synthesized a sequence of ultrathin copper sulphide nanosheets using the van der Waals epitaxy method,[110] and non-volatile memory behaviors were demonstrated by the as-synthesized materials. Owing to the high activity and low migration barrier energy of the Cu^{2+} ions in ultra-thin 2D copper sulfide crystals, the memristor displayed a series of advantages, such as a low switching voltage of about 0.4 V, fast switching speed, excellent stability of the switching characteristics, longer cycle life and a wide range of operating temperatures (80–420 K), as shown in Fig. 9d. The retention performance and cycle life of the memristor at different temperatures were tested, as shown in Fig. 9e. Moreover, this 2D-semiconductor-based memristor exhibited excellent memristive performance. Recently, a 2D MoSe memristor was fabricated using a non-destructive *in situ* technology by Bala *et al.*[111] It involved the controlled diffusion of selenium in molybdenum predeposited in a pattern, producing Mo//Mo:Se stacks and a 5 × 5 crossbar memristor array. This memristor showed a low switching voltage ($\sim$1.1 V), high endurance ($>$250 cycles) and excellent retention ($>$15 000 s). The proposed *in situ* technology can simplify the fabrication process and minimize the number of required stages. In 2021, a filamentary-type memristor with P-type selenium sulfide as the functional layer was prepared by Lu *et al.*[112] This memristor used Ag and Pt as the electrode materials, and SnS was maintained in the thickness range of 10–40 nm, as seen in Fig. 9f. This device exhibited good resistive-switching performance, such as a low switching voltage of about 0.2 V, a fast switching speed of 1.5 ns (Fig. 9g), and an ultra-large on/off ratio of up to 10^8. A highly reproducible threshold-switching behavior between HRS and LRS over multiple cycles was observed *via* the *I*–*V* curves shown in Fig. 9h. The chip-scale simulations of memristors with a feature size of 50 nm and based on a high-density crossbar array showed a high learning accuracy of 87.76% for image classification, as shown in Fig. 9i.

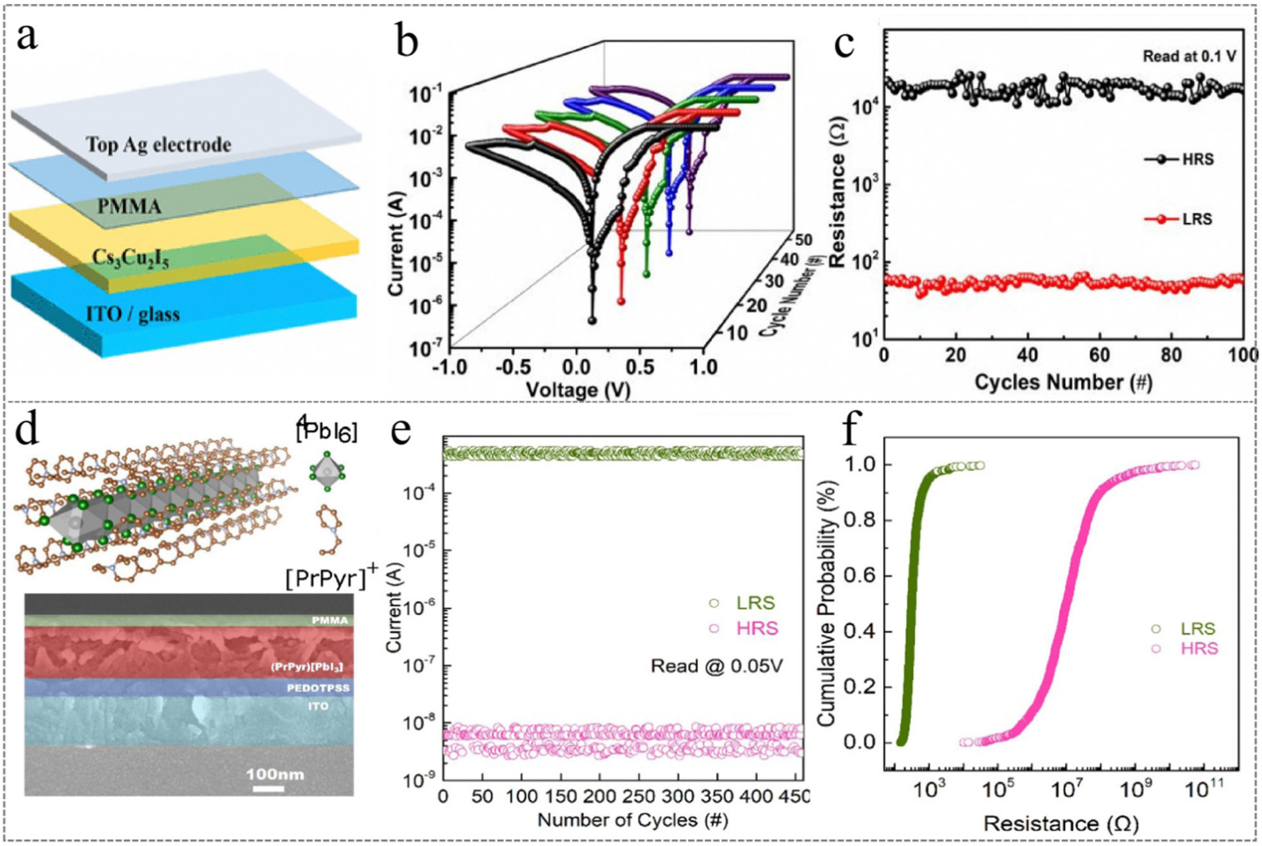

Fig. 8 (a) Schematic of the memristor with the Ag/$Cs_3Cu_2I_5$/ITO structure. (b) The *I*–*V* characteristic curves of the memristor over 50 sweeps. (c) The endurance test result of the Ag/PMMA/$Cs_3Cu_2I_5$/ITO memristor at a read voltage of 0.1 V. Panels (a–c) are reproduced with permission.[107] Copyright 2020, American Chemical Society. (d) The single-crystal structure of 1-D (PrPyr)[PbI_3] and the SEM image of the memristive device. (e) Endurance test over 450 switching cycles at a read voltage of 0.05 V. (f) The cumulative probability distribution of the HRS and LRS *via* 1024 devices. Panels (d–f) are reproduced with permission.[108] Copyright 2021, Nature Publishing Group.

Different from the 2D material-based memristors made by the traditional mechanical stripping method, Liu *et al.* fabricated a memristive device with the Ti/$HfSe_xO_y$/$HfSe_2$/Au crossbar structure based on 2D $HfSe_2$.[113] This 2D memristive device exhibited excellent forming-free resistive-switching performance, including a fast switching speed (<50 ns), a low operating voltage of about 3 V, a large switching window (10^3), and outstanding data retention performance, as shown in Fig. 10a. Besides, a smaller operating current of 100 pA and a low power consumption of about 0.1 fJ were obtained with the Ti/$HfSe_xO_y$/$HfSe_2$/Au memristor (Fig. 10b), which are much lower than those of other Hf–O based memristors. To further improve performance, Li *et al.* demonstrated a practical method for implementing memristors based on polycrystalline $HfSe_2$ thin films in neural network hardware.[114] A low switching voltage of ~0.6 V and a low switching energy of 0.82 pJ were demonstrated by the as-prepared device. When the switching cycle number exceeded 500, an endurance test with a resistance ratio of 100 was obtained, as shown in Fig. 10c. In addition, the simulation of synaptic weight plasticity was achieved using the as-prepared memristor device, and the simulation results of the artificial synapse under different pulse amplitudes are shown in Fig. 10d. In image recognition, the artificial neural network based on the 2D $HfSe_2$ memristor demonstrated high accuracy (93.34%) and a narrow error distribution of 0.29% (Fig. 10e), achieving a high power efficiency of more than 8 trillion synapses per watt per second during operations. At present, the limited repeatability of the resistive-switching behavior and the high energy consumption of the memristor device greatly inhibit the application of synaptic devices in the field of neuromorphic computing. In 2021, Li *et al.* prepared a memristor based on a heterogeneous grain boundary using 2D $PdSe_2$ as the functional layer.[115] The resistive-switching behaviour of the Ti/$PdSe_2$/Au memristor at different e-beam dosages is shown in Fig. 10f. This device exhibited anomalous resistive switching behavior in two fully interchangeable reset modes, as seen in Fig. 10g. The conductive mechanism of the device was local phase transition caused by electron beam irradiation, which formed an uneven grain boundary, and the formation of conductive filaments was induced by residual filaments along the grain boundary. Compared with the total-reset mode, the memristor exhibited increased switching change by 6 times when working in the quasi-reset mode (Fig. 10h), and it had a lower set voltage of about 0.6 V, long retention time, and a programmable multi-resistance state. The quasi-reset mode of the $PdSe_2$-based memristor was applied in neuromorphic computing, realizing

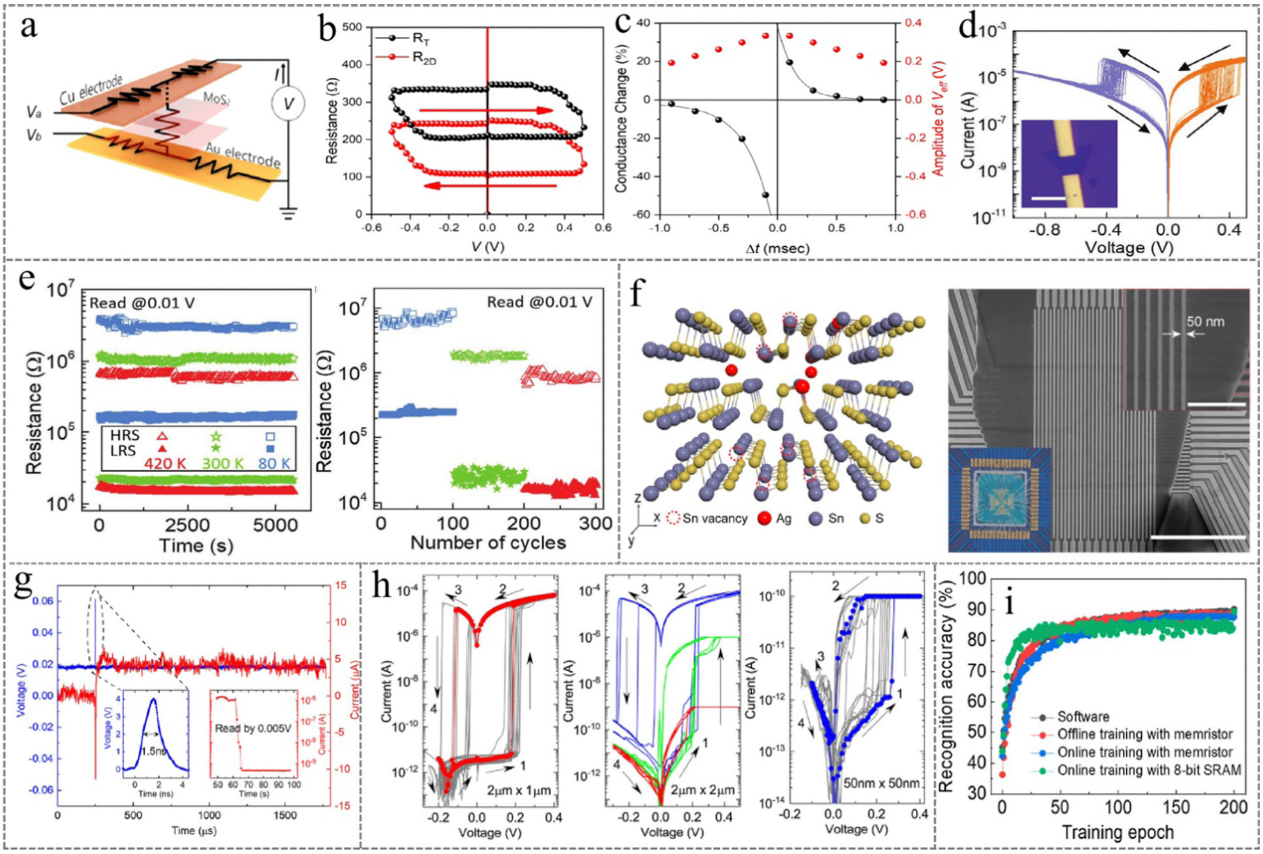

Fig. 9 (a) The memristive device with the Au/MoS$_2$ double layer/Au structure. (b) The measured resistance as a function of applied voltage. (c) The demonstration of STDP, the measured conductance of the memristive device and the effective voltage amplitude as a function of time. Panels (a–c) are reproduced with permission.[109] Copyright 2019, American Chemical Society. (d) The I–V curve of the CuSe-based memristor during 100 cycles, and the inset shows an optical microscopic image of the CuSe-based memristor. (e) The retention performance test for LRS and HRS under a temperature gradient (left) and the endurance performance of the CuSe-based memristor (right). Panels (d–e) are reproduced with permission.[110] Copyright 2022, Wiley-VCH. (f) The crystal structure of SnS and the SEM image of the memristor with a 32 × 32 high-density memristive crossbar array; the inset is an optical image of the chip. Scale bar, 1 μm. (g) The ultra-fast switching curve of the memristive device was read at a voltage of 0.02 V under a 4 V/1.5 ns voltage pulse. (h) The resistive switching behavior of the Ag/SnS/Pt memristor without current compliance (left) and with different current compliances (middle). The figure on the right exhibits the volatile resistive-switching feature of a device with the size of 50 nm × 50 nm. (i) The simulated classification accuracy results of the memristive device with the Ag/SnS/Pt structure for different images. Panels (f–i) are reproduced with permission.[112] Copyright 2021, American Chemical Society.

the simulation of synaptic plasticity and the implementation of the crossbar-array architecture under multimodal memory (Fig. 10i).

2.1.4 Hexagonal boron nitride (h-BN). It is well-known that the rapid development of 2D material synthetic routes and preparation technologies has promoted great breakthroughs in micro/nanoelectronic devices and brought about significant progress in the field of semiconductor research. Hexagonal boron nitride (h-BN) has superior chemical, mechanical and optical characteristics, along with the potential to overcome the size limit of nano- and even sub-nanometer to avoid the use of thick and hard materials in multi-terminal devices. Atomically, thin h-BN or van der Waals heterostructures can improve the reliability, performance, and functionality of memory devices. Chen *et al.* used h-BN as the functional material to fabricate a resistive-switching device with crossbar arrays and applied it to an artificial neural image-recognition network.[116] This h-BN memristor with a vertical Ag/h-BN/Ag structure exhibited low cycle-to-cycle and device-to-device variability of 1.53% and 5.74%, respectively, as shown in Fig. 11a. The measured I–V characteristics over 120 cycles are depicted in Fig. 11b, and the bipolar resistive-switching behavior of the h-BN memristor showed a high yield of ∼98%. Besides, the as-prepared Ag/h-BN/Ag device demonstrated an ultra-high on-off ratio of up to 10^{11} and an ultra-low setting energy consumption of 8.8 pJ, as shown in Fig. 11c. Recently, Kumar *et al.* used multilayer h-BN as the functional layer to prepare a memristor crossbar array, which demonstrated bipolar resistive-switching characteristics,[117] as shown in Fig. 11d. Further, it combined the 2D h-BN crossbar array with CMOS circuits to implement extreme machine learning algorithms, decoding functions, and classification demonstrations for complex audios, images, and other tasks. Fig. 11e shows the implementation of the system architecture based on the memristor decoder chips. In 2021, Mao *et al.* fabricated a non-invasive memristive device with the Au/h-BN/Au structure using the water-assisted metal transfer method by physically assembling Au electrodes onto layered h-BN.[118]

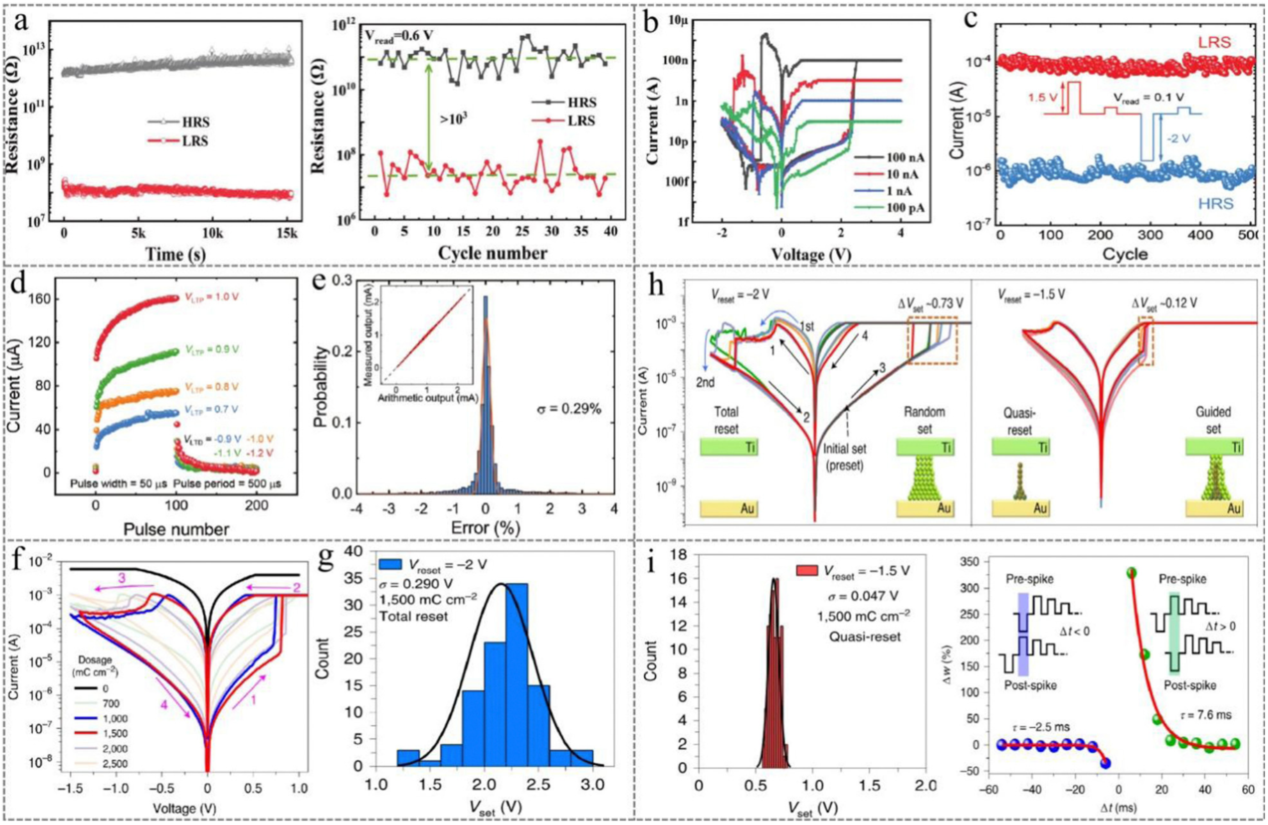

Fig. 10 (a) The retention test of HRS and LRS at 0.1 V (left), and the measurement of HRS and LRS under 100 nA operation current at a read voltage of 0.6 V (right). (b) The nonvolatile resistive-switching behavior at different compliance currents (CC). Panels (a and b) are reproduced with permission.[113] Copyright 2021, Wiley-VCH. (c) The endurance test over 500 cycles. (d) The LTP performance under positive/negative pulse training. (e) The corresponding error distribution between the measured results and the arithmetic results. Panels (c–e) are reproduced with permission.[114] Copyright 2022, Wiley-VCH. (f) The resistive-switching behaviours of the Ti/PdSe$_2$/Au memristive device under different e-beam dosages. (g) The interchangeable reset mode of the PdSe$_2$ memristor under e-beam irradiation at −2 V. (h) The *I–V* curves of the PdSe$_2$-based memristor during 100 cycles while operating in the total-reset mode (left) and the quasi-reset mode (right). (i) STDP simulation using the quasi-reset modes of the synaptic memristor. Panels (f-i) are reproduced with permission.[115] Copyright 2021, Nature Publishing Group.

Non-polarity and threshold switching could be realized by adjusting the current level, which was used as the logic gate and latch to realize logical operation for memory calculation, as shown in Fig. 11f. Yang *et al.* reported radiofrequency switching in the millimeter-wave range using a hexagonal boron nitride memristor with the Ag/h-BN/Ag structure.[119] This memristor showed excellent nonvolatile bipolar resistance-switching characteristics, including a high on/off ratio ($\sim 10^{11}$) and a low switching voltage (<0.34 V). It also exhibited pulse-switching characteristics when set at high speed with a very low power of 0.23 W and energy consumption of 1.2 nJ. An excellent 0.50 dB insertion loss and isolation above 23 dB were observed in advanced millimeter-wave-frequency measurement and calibration. This device shows great application prospects in future reconfigurable wireless and 6G communication systems.

2.1.5 Ferroelectric materials. As one of the most potential nonvolatile memristors, ferroelectric memristors have been widely applied in information storage, logic computing, neuromorphic computing, image recognition and artificial intelligence. They can be used as flexible electronic components in next-generation biomedical applications and can simulate the integrated brain functions of storage and computing to adapt to the rapid development of next-generation artificial intelligence. The continuous intermediate state of ferroelectric polarization can be obtained by adjusting the amplitude or duration of the applied voltage pulse.[120] The reversal of the ferroelectric domain does not cause the local migration of ions or defects, thus resulting in high durability ($>10^{14}$ cycles).[121] According to the geometric structure, organic ferroelectric synapses are mainly divided into two types: two-terminal synaptic devices and three-terminal synaptic devices. In a two-terminal ferroelectric synaptic device, the ferroelectric layer is usually sandwiched by two metallic electrodes. This device will provide a real-time conductance update and read the synaptic weight from the other electrode when a presynaptic signal is applied to one electrode so that the prickle signal is transferred from the presynaptic terminal to the postsynaptic terminal. In three-terminal ferroelectric synaptic devices, the presynaptic processes are usually imposed on the gate electrode, thus affecting synaptic plasticity.[122] At present, ferroelectric materials, including inorganic ferroelectrics,[123] organic ferroelectrics,[124] and molecular ferroelectrics,[125] have been used in information storage and artificial synaptic devices

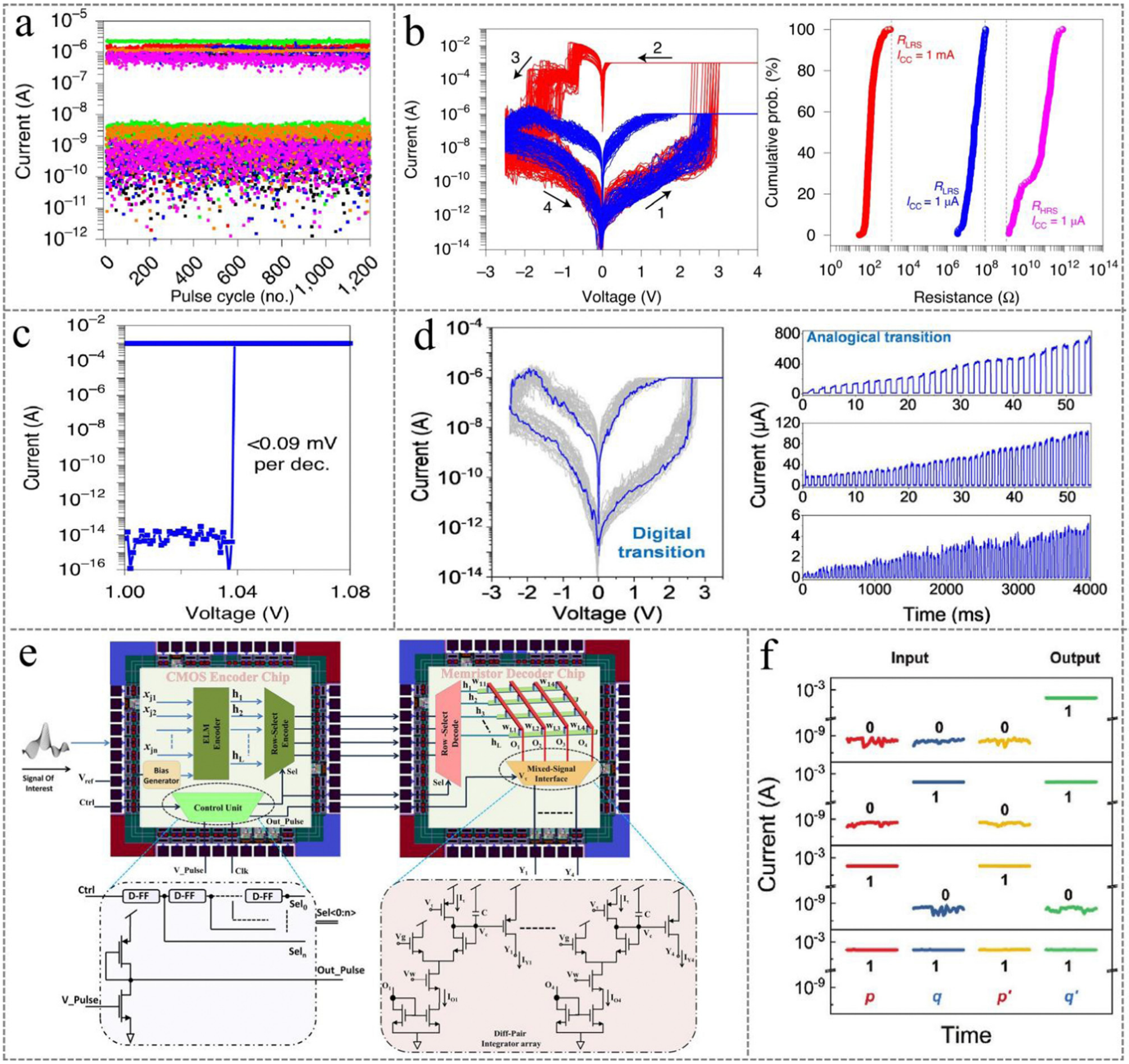

Fig. 11 (a) The endurance test of the Au/Ag/h-BN/Au memristor over 1200 programming cycles. (b) The I–V characteristics measured over 120 cycles show the bipolar resistive-switching behavior of the h-BN memristor (left) and the cumulative distribution of HRS and LRS were measured over 1500 cycles (right). (c) The threshold-type resistive switching behaviour of the Ag/h-BN/Ag memristive device. The high I_{LRS}/I_{HRS} current window indicates excellent resistance recovery. Panels (a–c) are reproduced with permission.[116] Copyright 2020, Nature Publishing Group. (d) The measured I–V characteristics exhibit nonvolatile bipolar resistive-switching behavior. (e) A comparison of the system architecture diagrams of the CMOS encoder chip and the memristor decoder chip. Panels (d and e) are reproduced with permission.[117] Copyright 2022, Nature Publishing Group. (f) Logic implementation based on the Au/h-BN/Au memristor array for four input conditions. Panel f is reproduced with permission.[118] Copyright 2022, Wiley-VCH.

to simulate synaptic function. In particular, organic ferroelectric synapses are suitable for different functional applications according to the actual needs on different occasions and can be used to establish cognitive, memory, visual, tactile and other perception and information processing systems.[125] In recent years, van der Waals ferroelectric materials have shown significant potential for utilization in complex circuits, energy-saving integration, brain-like computing systems and storage logic operations. Among them, van der Waals ferroelectric In_2Se_3 has unique out-of-plane and in-plane polarization, due to which the In_2Se_3-based memristor device has realized multi-directional resistance switching performance. Gu *et al.* fabricated a planar ferroelectric memristor based on van der Waals α-In_2Se_3,[126] which could be continuously tuned over three orders of magnitude and displayed resistive-switching behavior. The microscopic mechanism of multidomain formation and the in-plane energy barrier between the domains were also revealed. In 2021, Xue *et al.* reported an emerging ferroelectric α-In_2Se_3 memristor that can be used to implement heterosynaptic plasticity and a heterogeneous synaptic characteristic with a resistance ratio of 10^3, which is superior to other similar memristive devices.[127] This memristor achieved resistive switching by adjusting the polarization channel of α-In_2Se_3. The neural network constructed using the α-In_2Se_3-based memristor realized supervised learning and unsupervised learning with high image recognition accuracy. Recently, Xue's group employed a planar van der Waals ferroelectric α-In_2Se_3 memristor to explore the mechanism of ferroelectric resistive-switching behavior.[128] Through interface manipulation, the device realized a large on/off ratio greater than 10^4, and a ferroelectric resistance-switching mechanism contrary to the general explanation was proposed. They pointed out that the ferroelectric resistive-switching behavior was determined by ferroelectric polarization and the Schottky barrier height, and its initial Schottky barrier height and polarization at both ends shield the charge.

In addition, other types of ferroelectric materials have also been used to prepare nonvolatile memristors. In particular, with the investigation of ferroelectric materials, researchers are very interested in exploring next-generation nonvolatile ferroelectric memristors, which are expected to achieve high-density storage and arithmetic operations. Yan *et al.* fabricated a novel ferroelectric thin-film memristor with a $BaTiO_3$-CeO_2/$La_{0.67}Sr_{0.33}MnO_3$/$SrTiO_3$ vertically aligned nanocomposite structure on a monocrystalline Si substrate with $SrTiO_3$ as the buffer layer.[129] By improving the experimental conditions, vertically arranged epitaxial nanostructures were obtained, and the resistance characteristics were improved. Finally, the multi-value storage functions of these five states were obtained, and robust durability up to 10^9 cycles was observed. Moreover, the device successfully simulated the function of artificial synaptic paired-pulse facilitation. The algebraic computing capability at fast pulses with a width of about 50 ns was demonstrated. When applied for the recognition of datasets based on CNN, it achieved recognition rates of 90.03% and 92.55% for online and offline learning, respectively. In particular, the photoelectric synapse is also a novel type of artificial synapse combining optical pulse excitation and electrical pulse excitation, forming an important part of neuromorphic hardware development. Zhong *et al.* reported a double-stranded ferroelectric artificial synapse based on a photoelectric co-excited state,[130] which used ultraviolet irradiation to generate excitatory postsynaptic currents and photoelectric dual controlled synapses. The memristor employed a training method based on ultraviolet excitation and ferroelectric enhancement, which greatly reduced the number of training pulses and increased synaptic plasticity. By using this memristor for the construction of convolutional neural networks, a 98.8% accuracy of data set recognition could be achieved.

Recently, Lin's group demonstrated improved characteristics of memristors with ferroelectric tunnel junctions (FTJs).[131] In this work, a high-performance ferroelectric tunnel junction synapse based on the Ag/PZT/NSTO (Nb: 0.7 wt%) heterostructure was reported, in which (111)-oriented $PbZr_{0.52}Ti_{0.48}O_3$ (PZT) is with an ultrathin thickness of $\sim$1.2 nm was designed and constructed. This device is close to the morphotropic phase boundary and exhibited multiple resistive switching and ultra-fine ferroelectric behaviors with ultra-high performance, including 256 states and 8-bit high-accuracy display (Fig. 12a), a sufficient conductance dynamic range ($\sim$100×), remarkable endurance over 10^9 cycles (Fig. 12b), and ultra-low write power consumption. Fig. 12c shows the analog manipulation within the duration of $\sim$ 630 ps and a series of pulse voltages less than 5 V. The CNN simulated based on the device could achieve learning and image-recognition accuracy up to $\sim$94.7%, which is very close to the result of $\sim$95.6% obtained by the convolutional neural network software, as shown in Fig. 12d. In 2022, Gao *et al.* fabricated a novel three-terminal trihalide perovskite ($MAPbI_3$) memristor with top-gate field effect geometry using the ferroelectric material poly-vinylidene fluoride-trifluoroethylene as the functional layer,[132] as shown in Fig. 12e. Different working modes (volatilization and non-volatilization) could be created by modulating ion transport and the migration barrier at the switching interface of the non-filamentous perovskite memristor, which was able to simulate biological nociception for perceived pain and inhibited pain signals. Besides, the memristor could work in an environment with 7.8% cycle fluctuation and a current lower than 100 nA. The *I–V* curves of the memristor established over 100 cycles show analog switching characteristics with excellent cycle-to-cycle uniformity compared with a filament-based memristor, as shown in Fig. 12f. Recently, Cai *et al.* prepared a double-terminal ferroelectric synapse memristive device based on a disopropylammonium bromide/copper phthalocyanine heterostructure.[133] The memristor utilized a copper phthalocyanine (CuPc) thin film (50 nm) as the semiconductor layer, and a high-quality disopropylammonium bromide thin film of thickness 500 nm was fabricated *via* a surface tension-assisted drop-casting method. The interfacial resistance was modulated by controlling the blocking effect of the polarization of the semiconductor, achieving synaptic features, including STDP, as shown in Fig. 12g. This optoelectronic synapse based on the ferroelectric/semiconductor interfacial memristor was applied in the construction of an ANN, which showed high image-recognition accuracy. Fig. 12h shows the variation in image-classification accuracy with noise between the weight quantification and unquantized models, and the structure and principle of the artificial neural-network-based image sensor are shown in Fig. 12i.

Recently, some progress has been made in the application of ferroelectric memristors in neural networks. Wang *et al.* fabricated a three-terminal memristor with the Ag/WO_x/$BiFeO_y$/FTO structure by magnetron sputtering.[134] This device showed favourable nonvolatile resistance-switching memory behavior, which meets the requirements for high-density information storage. Liu *et al.* demonstrated a $BiFeO_3$ ferroelectric thin film of several-nanometer thickness for manipulating in-plane charged domain walls.[135] The voltage control of the domain wall position in the $BiFeO_3$ plane produced multiple nonvolatile resistance states in the W/$SrRuO_3$/$BiFeO_3$/$SrRuO_3$/Nb–$SrTiO_3$ ferroelectric memristor, thus realizing the key functional characteristics of a memristor with several unit-cell thickness. This promotes a better understanding of ferroelectric switches and provides a new strategy for creating unit-cell-scale

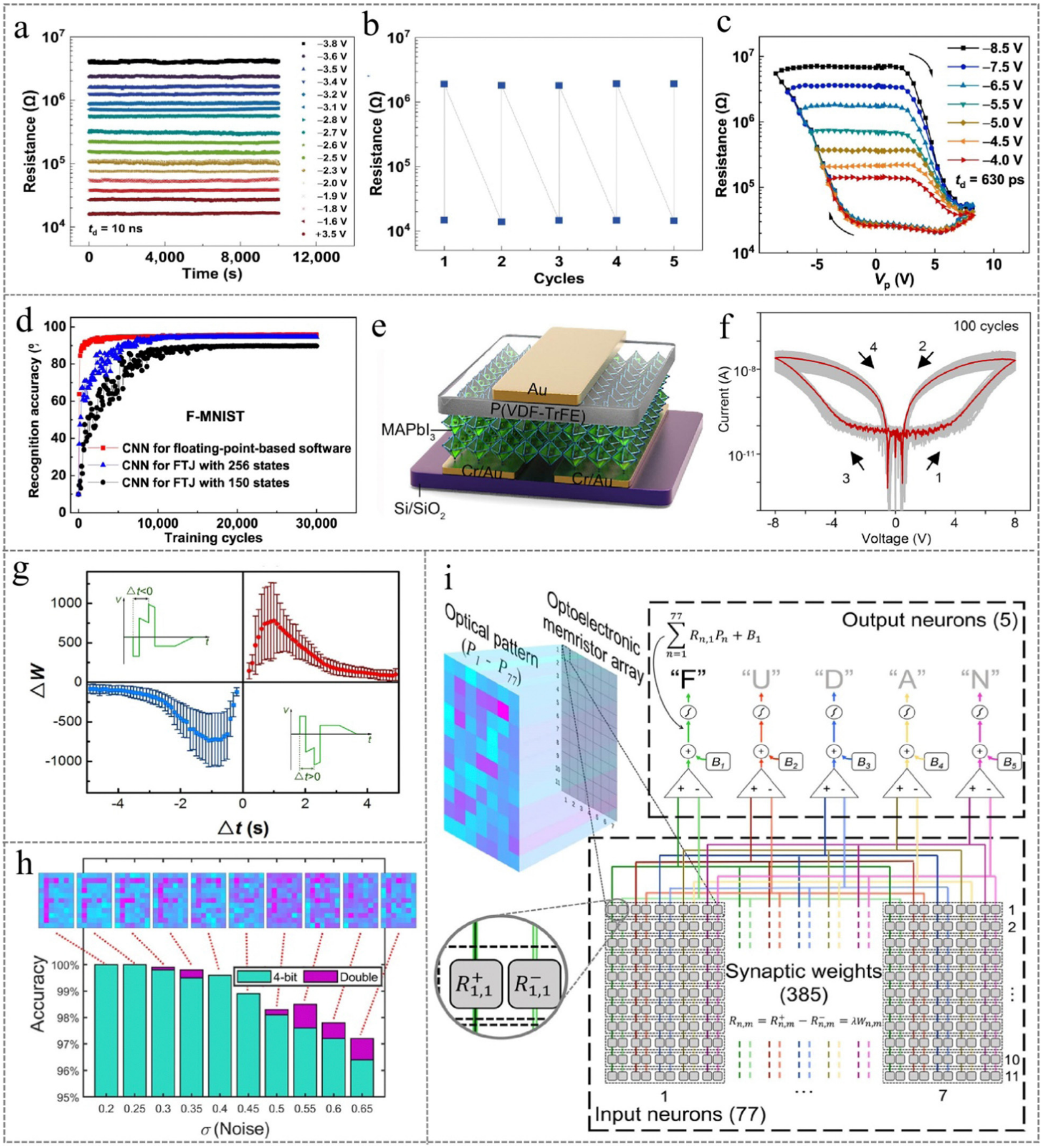

Fig. 12 (a) The enhancement and suppression of 256 conductance states over 100 dynamic ranges by increasing a series of pulse voltages. (b) Five resistance-switching cycles of the ferroelectric tunnel junction with a (111)-oriented $PbZr_{0.52}Ti_{0.48}O_3$ barrier after the 10^9 cycles. (c) The resistance measured at 0.05 V as a function of pulse voltage with a pulse duration of ∼630 ps. (d) The simulation results of the neural network based on different conductivity states and floating-point-based software learning. Panels (a–d) are reproduced with permission.[131] Copyright 2022, Nature Publishing Group. (e) The schematic of the perovskite bimodal memristor. (f) The *I*–*V* curves measured based on the Au/MAPbI$_3$/Au memristive device. Panels (e and f) are reproduced with permission.[132] Copyright 2022, AIP Publishing. (g) The STDP simulation of the artificial synaptic devices. (h) The classification accuracy varies with noise; the green bars represent the accuracy after 4-bit weight quantization, and the purple bars represent the accuracy of the unquantized model. (i) The structure and principle of the artificial neural network image sensor. Panels (g–i) are reproduced with permission.[133] Copyright 2022, Nature Publishing Group.

devices. Besides, a memristor with the CeO$_2$/Nb–SrTiO$_3$ heterojunction structure[136] exhibited a real-time conductance-tuning function with the application of a positive/negative pulse sequence. This memristor showed excellent conductance-switching behavior and a high switching ratio (10^5), further realizing the simulation of bio-synaptic functions. In addition, the CNN constructed using this memristor was used to identify the electrocardiogram data set, and the recognition accuracy was up to 93%, while the recognition accuracy for handwritten numbers reached 96%. Gao *et al.* proposed a three-terminal memristor with a top-gate field effect using a ferroelectric material, namely poly(vinylidene fluoride-trifluoroethylene), as the resistance layer.[132] Two different operation modes (volatile and non-volatile) were realized by adjusting the ion transport and contact barrier at the switching interface of the ferroelectric memristor. In addition, the memristor showed ideal resistance-switching performance (high yield of 88.9%, cycle-to-cycle variation of 7.8%, and low operating current of less than 100 nA). At the same time, this device realized the simulation of bio-nociception and blocked states.

2.2 Organic-memristor-based neural networks

2.2.1 Natural biomaterials. Due to the high biocompatibility between biomemristors and biological tissues, they can solve the inherent limitations of traditional memory-element-based artificial perception systems in implantable applications. Research on memory effects in organic materials began in 1979 when switching between different resistance states was observed in polystyrene and copper-tetracoquinedimethane (Cu-TNCQ) films.[137] Since then, significant progress has been made on organic memory devices. Natural biomaterials mainly include plant materials, polymers, biomolecules, proteins and their complexes, sugars and deoxyribonucleic acid (DNA), *etc.* In recent years, many studies have been carried out on the preparation of memristors based on natural biomaterials. Fu's group demonstrated a diffusion memristor made from protein nanowires obtained from the bacterium *Geobacter sulfurreducens*,[138] and the structure of the memristor can be found in Fig. 13a. This memristor achieved a high switching ratio of 10^6 and a cycle number of 10^4, as shown in Fig. 13b. The simulation of neuromorphic structures, such as artificial neurons and synapses, was implemented in this work. Fig. 13c demonstrates a bio-voltage artificial synapse constructed using a protein-nanowire-based memristive device. In addition, an unconventional right-angle resistance-like switching behavior was observed as a switching medium by Chang *et al.*[139] This memristor had a simple Ag/fibroin-AgNCs/ITO sandwich structure and could operate for more than 300 cycles at an ultra-low operating voltage of 0.03 V with an extremely high resistance memory window of 10^7, as shown in Fig. 13d. The *I–V* curves of the memristor at bending angles -60° and 60° are shown in Fig. 13e, which exhibits stable resistive-switching behavior in both bent and flat conditions. Further, Hussain *et al.* proposed an environmentally friendly nanocomposite-membrane-based memristive device with good bipolar resistance-switching behavior, and this device was composed of silver nanoparticles and cellulose nanocrystals (CNC).[140] This memristive device performed continuous resistance modulation to simulate artificial bio-synapses, proving to be conducive to nonvolatile digital memory and neuromorphic computing. Due to the electrochemical formation/fracture of conductive Ag filaments in the nanocomposite layer, the biomemristor exhibited a large on/off resistance ratio of 10^4 and an ultra-low SET and RESET voltage of 0.2 V. In particular, this device shows reliable digital and analog resistance switching properties towards the multifunctional application of neuromorphic systems.

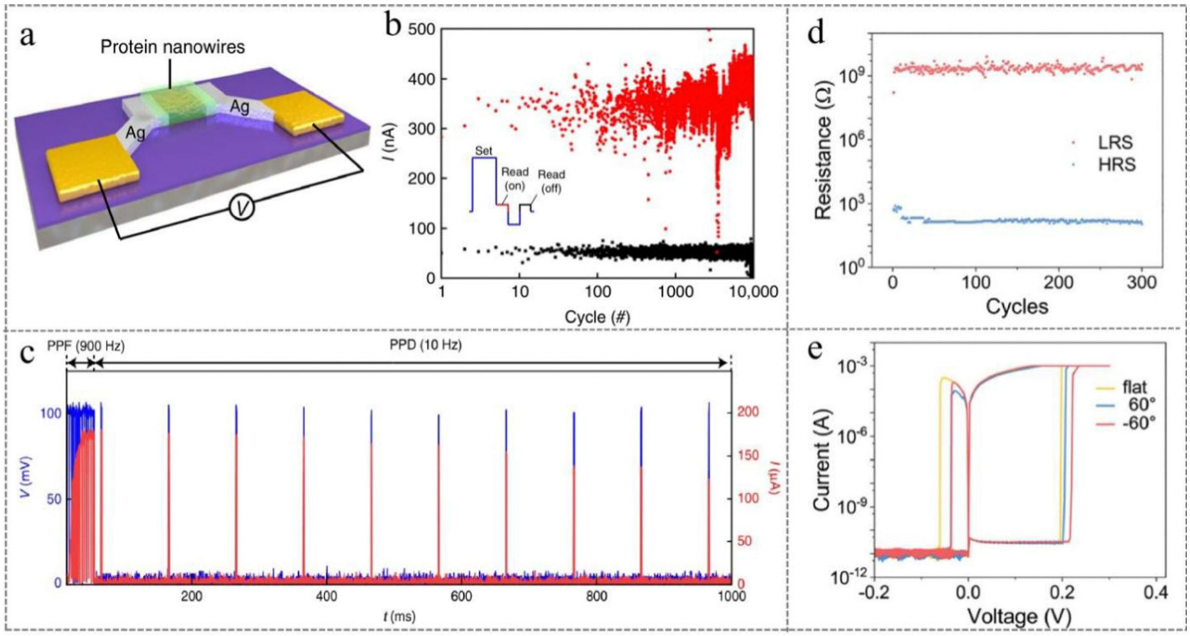

Fig. 13 (a) The schematic of the memristive device with an Ag/protein nanowires/Ag structure. (b) The current of the vertical device at HRS and LRS over 10^4 cycles. (c) The conductance modulation of the protein-nanowire-based memristor. Panels (a–c) are reproduced with permission.[138] Copyright 2020, Nature Publishing Group. (d) The endurance performance of the memristor. (e) The flexible performance of the device involving the resistive switching behavior of the memristor in the bent state. Panels (d and e) are reproduced with permission.[139] Copyright 2021, Wiley-VCH.

Biological systems are usually operated at a low voltage, but the operating voltage of traditional memristors is relatively high, which is not applicable to energy-saving biological systems. To address this issue, Zhao *et al.* demonstrated a high-performance filament-based threshold-switching (TS) memristor, which exhibited an on-current of 1 mA, a low threshold voltage of 0.17 V, and high selectivity of 3×10^6.[38] In addition, this memristive device showed excellent uniformity and stability, demonstrating typical bio-synaptic STP, including facilitation to the pulse, even at high humidity (80%) and a high temperature (70 °C).

In addition to using proteins as the functional layer material in memristor devices, many studies have also used sugars for the preparation of memristors. Min *et al.* reported a memristor prepared using the biomaterial chitosan-based solid polymer electrolyte (SPE).[141] They used the SPE-chitosan as the functional layer of the double-terminal memristive device with a Ti/SPE-chitosan/Pt structure. Due to the electrochemical reactions between the electrolyte and metal ions, this device exhibited stable bipolar resistive-switching behavior with excellent durability for 500 cycles. The *I–V* characteristics of multilevels per cell with bipolar resistive switching were also achieved by adjusting the SET current, and the STP and LTP of bio-synapses were also simulated. In 2021, a wafer-grade acid polysaccharide thin film with significant transient properties has been reported as a promising memristive material.[142] This memristor is independent, lightweight, and could be completely dissolved in deionized water within 3.5 s. The ion-constraining ability of the acid polysaccharides allowed the cations to interact with ionizable acid groups, thus enabling atomic manipulation. It has been reported that the individual device could generate 16 highly controllable and mutually independent quantized conductance (QC) states with nonvolatile properties, and QC switching could be performed at an ultra-fast speed of 2–5 ns with a low energy consumption of 0.6–16 pJ. Furthermore, the encoding/decoding and nonvolatile fundamental Boolean logic were designed and implemented as they are important for developing nanodevices with quantum effects. Zhang's group developed a chitosan (CS)-prototype graphene oxide (rGO) interpenetration network electrolyte and applied it as the functional layer of a memristive device to develop a reproducible low-power polymorphic biomemristor.[143] The designed cross-through network structure enhanced the stability of the device and improved the ionic conductivity. The biomemristor showed stable bipolar resistance-switching behavior with good stability, reproducible polymorphic storage, and low programming power of 9.4 μW. Moreover, this device presented good biocompatibility and excellent deformation stability during 1000 bending cycles, confirming the possibility of the application of this high-performance biomemristor in artificial sensing systems.

Using natural biomaterials in the functional layer to manufacture electronic devices meets the requirements of sustainable green electronics and is also suitable for preparing biomemristors. Li's group demonstrated an organic memory synapse formed using dichloropalphthalocyanine, which was capable of switching conversion under the temperature of 300 °C,[144] as shown in Fig. 14a. In addition, the flexible device maintained stable resistance switching behavior after 50 consecutive mechanical bending cycles, as shown in Fig. 14b. Fig. 14c shows that the device could simulate a trainable and

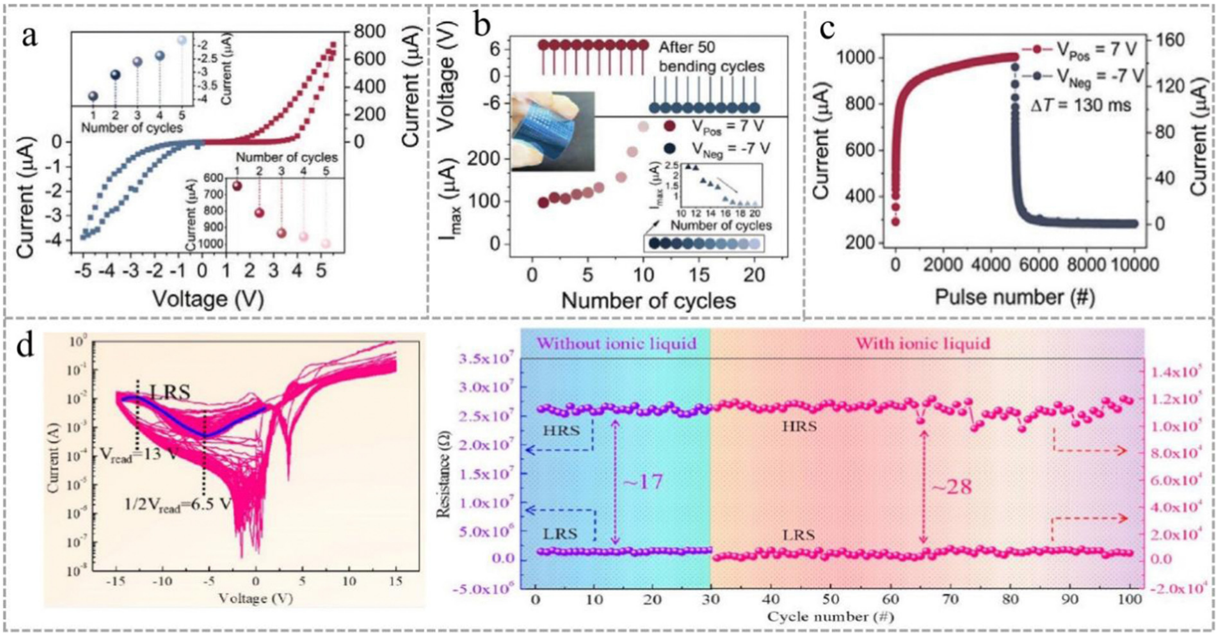

Fig. 14 (a) The *I–V* characteristics under positive and negative voltage sweeps before the cyclic bending test. (b) The change in current acts as a function of cycle number; the inset on the right indicates the change in current *versus* the number of sweep cycles under negative bias. (c) Current change under the continuous stimuli of 7 V/−7 V pulses corresponding to potentiation and depression, respectively. Panels (a–c) are reproduced with permission.[144] Copyright 2021, Wiley-VCH. (d) The cyclic test of HRS/LRS and the *I–V* nonlinear performance of the Mo/$C_{15}H_{11}O_6$-graphene/Mo device with an ionic liquid. Panel d is reproduced with permission.[39] Copyright 2021, American Chemical Society.

reconfigurable memristor array and perform image information processing. This finding provides a reference for the application of thermoelastic organic synaptic devices in neuromorphic computing. Recently, anthocyanin ($C_{15}H_{11}O_6$), a sustainable natural biomaterial, was used for ion and electron transport.[39] It could significantly modulate the capacitive-coupled memristive behavior of the as-prepared biomemristor. By inserting graphene into the biomaterial matrix, memory effect manipulation through graphene protonation was achieved. Finally, this device was applied to the 0T-1R array configuration, demonstrating the potential application of battery-like self-selected biomemristors in brain-inspired neuromorphic computing, data storage systems, and high-density device integration, as shown in Fig. 14d.

2.2.2 **Organic polymers.** In addition to natural biomaterials, organic polymers are another major category of organic materials that have been widely used in the research of memristor-based brain-inspired computing devices. However, it is undeniable that most organic–polymer solid-electrolyte-based memristive devices have poor reproducibility, durability and stability. In 2020, Yang *et al.* first demonstrated a novel polymer memristor using polyethyleneimine (PEI) as a solid electrolyte with thermally stable molecular groups and polar bond structures, which assisted ion migration in a large temperature range.[145] The sandwich structure of the Ag/PEI/Pt memristive device was designed to test the resistive-switching performance, as shown in Fig. 15a. The atomic-switching memristor exhibited a stable resistance-switching behavior at both room temperature and high temperatures with excellent retention and a high on/off resistance ratio of up to 10^5, as shown in Fig. 15b. Moreover, this device exhibited stable cycling performance in the temperature range from 25 °C to 150 °C. After 2000 bending cycles, it still exhibited excellent resistive switching performance at 150 °C, demonstrating that this device has great potential as a flexible electronic device for wearable applications (Fig. 15c). In 2021, Kim *et al.* demonstrated a hydrophobic fluoropolymer-based memristor that could be simply printed onto an organic transistor without damaging the underlying semiconductor layer,[146] and the device structure is shown in Fig. 15d. It was found the device had excellent stability and high mechanical durability even under repeated bending stress, as shown in Fig. 15e. Further, the artificial synapses proposed consisted of fluoropolymer-based memristors integrated with an organic transistor, and the hydrophobic fluorinated polymer was used as the functional layer of the memristor, preventing the diffusion of water to the transistor and thus greatly improving the stability of the device. In addition, the flexible artificial synapse with the 1T-1R configuration showed linear and accurately tunable multi-level conductance, achieving the capability of hardware-based neural networks (the image recognition accuracy was about 85%.), as shown in Fig. 15f. Furthermore, a two-terminal memristor based on the sandwich structure of Ag/AZB:PMMA/FTO was prepared using a common organic dye, azobenzene (AZB), as the functional layer of the device.[147] Fig. 15g shows that the device could achieve conversion between different dominant states with increasing voltage. In the low-voltage range, the device performed as a capacitance-dominated state (CDS) with a higher capacitance than the theoretical value (with a 10^4 improvement). In the high-voltage range, it was in a memristance-dominated state (MDS) with an HRS/LRS resistance ratio of $\sim 10^4$ and could achieve logical operations, as shown in Fig. 15h. Although artificial synapses are promising electronic components for constructing neuromorphic computing systems, they suffer from poor linearity and limited conduction states. Recently, a memristor based on $AgNO_3$-doped iota-carrageenan (ι-car) with an Ag/$AgNO_3$: ι-car/ITO structure was prepared by Zhang *et al.* to solve the nonlinear limitation problem.[148] This memristor showed a higher linear conductance regulation capacity of $\sim 10^4$, richer conduction states over 2000, and lower power consumption of 3.6 μW compared with other memristors. The authors point out that the doping of $AgNO_3$ into ι-car suppressed the formation of Ag conductive filaments, thereby eliminating inhomogeneous Joule heating. Based on these findings, this device was applied for deep learning of handwritten digits and achieved recognition accuracy of 93.8% (ideal for 95.7%), as shown in Fig. 15i. Therefore, this work verifies the feasibility of using biopolymers for future high-performance computing and wearable/implanted electronic applications. Recently, Xiong *et al.* experimentally demonstrated a neuromorphic functional fluidic resistor using polyelectrolyte-confined fluidic structures, which feature the typical fingerprints of a memristor.[149] This memristor embodies a powerful ability to simulate the STP electrical pulse mode, and its retention time and energy consumption are comparable to those of ion channels in biological systems. Besides, this device can provide more advanced neuromorphic functions, which are difficult to achieve in solid-state devices. These characteristics facilitate the possibility of introducing specific chemical regulation pathways into neural morphological functions.

2.3 Challenges and strategies for memristor-based neural networks

At present, a series of progress has been made in the hardware implementation of mathematical models based on synapses, neurons and neural networks. The realization of artificial neural networks on chips mainly depends on the memristor, and the application of memristor dynamics in neural networks has achieved great development, such as first-order memristors, second-order memristors and dynamic memristors.[150] Among them, first-order memristors provide a wide variety and account for the majority; they can show continuous resistance changes when different amplitude voltage pulses are applied.[151] At present, some synaptic learning functions, such as STP, LTP and STDP, have been successfully demonstrated in these electronic synapses.[152,153] However, the modulation of first-order memristor conductance is only controlled by the applied external voltage, which results in some synaptic characteristics (such as the shape of presynaptic and postsynaptic voltage pulses) being not well simulated. Second-order memristors can simulate the time dynamics of bio-synapses through the ion drift and diffusion dynamics of metal species. In a

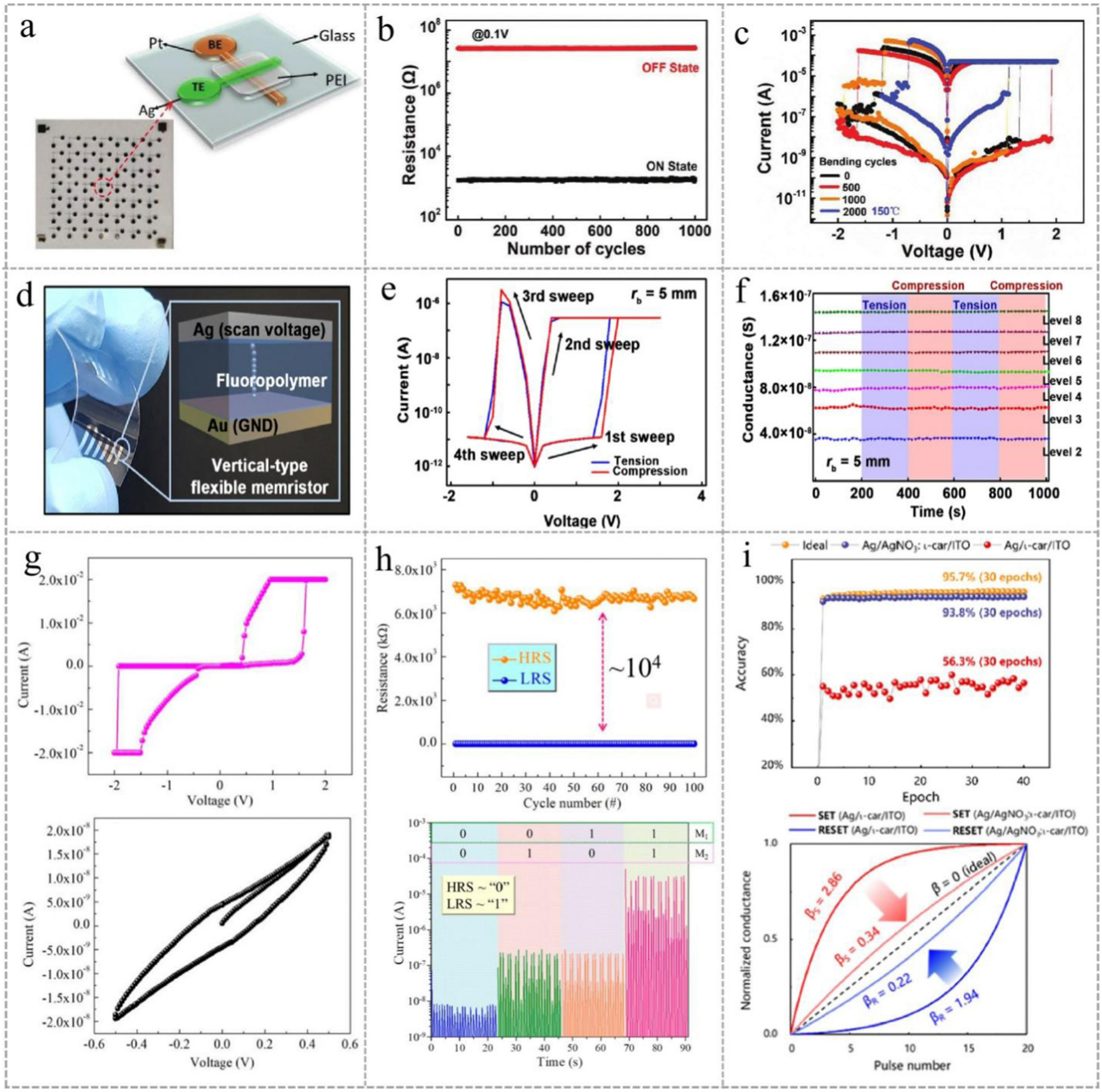

Fig. 15 (a) The schematic of the Ag/PEI/Pt memristive device. (b) The cycle performance of the memristive device at HRS and LRS during 1000 cycles at 0.1 V. (c) The *I*–*V* curves of the Ag/PEI/Pt/PI memristive device under repeated mechanical bending for 2000 times. Panels (a–c) are reproduced with permission.[145] Copyright 2020, Wiley-VCH. (d) The photographic image and device structure of the fluoro-polymer-based flexible memristor under bending deformation. (e) The *I*–*V* characteristics of the memristive device under bending stresses with a radius of 5 mm. (f) The reliable multilevel memory properties expressed *via* artificial synapses and its electromechanical stability at seven memory states. Panels (d–f) are reproduced with permission.[146] Copyright 2021, Nature Publishing Group. (g) The *I*–*V* characteristics of the memristive device at different voltages (0.5 V top, 1 V bottom). (h) The endurance test of the high/low resistance states and the logical operation of the Ag/AZB:PMMA/FTO memristive device at a read voltage of 0.25 V. Panels (g and h) are reproduced with permission.[147] Copyright 2022, American Chemical Society. (i) A comparison of the linearity of the weight update curves (bottom) and the recognition accuracy of the handwritten digits (top). Panel i is reproduced with permission.[148] Copyright 2021, American Chemical Society.

second-order memristor, the conductivity is controlled by some internal time mechanisms, and the relative timing information is captured by the second-state variables (thermal dissipation of oxygen vacancies in the conducting filament,[154] the decay of oxygen vacancy mobility,[155] the minimization of interfacial energy of the metal species,[156] and so on). Its activation and spontaneous decay following external spike stimuli provide an internal mechanism to encode the temporal spike information and thus enable natural modeling of the frequency responses. Currently, most second-order memristor devices can be used to simulate temporal synaptic performance on the chip. However, there are some significant obstacles to connecting neural networks with memristors, especially in situations where the stability of the device is critical to computational accuracy. In the process of conductance modulation, the memristor will demonstrate atomic-scale random defects and variations, among which uncontrolled ion migration in the memristor device has a great influence on the device-to-device and cycle-to-cycle variation, cycling endurance and dynamic range (on/off ratio). The uncertain drifts in the conductance state over time or environment change correlate with undesired changes in synaptic weight in neural networks. The emergence of non-ideal memristor characteristics has become the main factor that affects the learning accuracy of neural networks, and it has always been one of the main challenges faced by neural network-based systems.[157] Besides, the reliability concepts and material characterization methods for analog memristors vary widely, and generally accepted evaluation criteria are still lacking. At the same time, the complexity of the physical mechanism of analog resistive switching makes it difficult to study the mechanism of device reliability. This makes the cross-layer co-design from device to system/algorithm incomplete, thereby also restricting the application of memristors in neural networks.

In order to improve the application of memristors in neural networks, researchers have tried to provide some feasible solutions from the aspects of process technology, innovative materials, the structure of the memristor and the programming scheme. Some methods have been proposed to reduce the retention loss, enhance retention and improve the on/off ratio by adding annealing operation and metal doping.[158,159] Recently, some researchers have also focused on improving the memristive properties of memristors. Sung *et al.* proposed a capacitance-dependent voltage division analysis to suppress the hidden current generated by adjacent units in a 3D memristive array.[160] This method effectively reduced the leakage of the interface capture current between the resistive switching and metal layers, resulting in excellent retention ($>5 \times 10^5$). Liu *et al.* synthesized wafer-scale ultrathin 2D imine polymer films with controllable thickness using the Schiff base polycondensation reaction method, thus improving the preparation method of memristors.[161] This free-standing porous film exhibited a feasible switching performance (endurance and data retention up to 200 cycles and 8×10^4 s, respectively). Yin *et al.* successfully realized current limitations by controlling the space charge in a 2D-Bi_2Se_3-based memristor using a damage-less ion implantation technology by using ultra-low energy plasma.[162] The memristors exhibited stable resistive switching behavior, including a high resistive switching ratio of 10^4, excellent cycle durability up to 300 cycles, and excellent retention ($>10^4$ s). Recently, Kim *et al.* proposed a new material stacking method in order to improve the switching performance of memristors.[163] A memristive cross-array stack with the $Pt/Ta_2O_5/Nb_2O_{5-x}/Al_2O_{3-y}/Ti$ structure exhibited a high retention characteristic (retention time over 10^5 s at 150 °C). Su *et al.* designed a new multilevel nonvolatile lead-free cesium halide memristor with lead-free cesium halide in the MoO_x interface layer as the functional layer, and a highly uniform and reproducible memristor was obtained.[164] This device showed a long retention time ($>10^6$ s), high durability ($>10^5$), and an ultra-high on/off ratio of 10^{10}. Towards the improvement of the preparation method, Tang *et al.* demonstrated a solution-treated 2D-MoS_2 memristor array and realized 3D integration by stacking 2D-MoS_2.[165] This memristor could adjust the switching characteristics through the diffusion of sulfur vacancies between the thin sheets, resulting in excellent durability, long memory retention, low device difference, high analog on/off ratio and linear conductance update. Generally, there are two main research directions to improve the performance of memristors at the material level. One is to explore growth conditions and modification processes to improve the physical properties and interface quality of the memristive materials, and the other is to explore new materials with unique properties through experiments, software simulation and machine learning.[24,166]

3. Summary and Outlook

Since 2010, the integration of crossbar arrays and memristors has been attempted to implement hardware neuromorphic computing.[153] The large-scale and high-density neural network integration of memristor devices is crucial for logic computing,

Table 1 Comparison of some representative memristors based on different materials

Devices	Thickness of functional layer (nm)	On/off resistance ratio	Retention time (s)	Endurance (cycles)	Ref.
Pt/h-BN/Ag	0.33	10^7	N	10^8	95
$Ag/PMMA/Cs_3Cu_2I_5/ITO$	500	10^2	10^4	100	107
$Ag/CsPbBr_3$ NCs/PTPO/PEDOT:PSS/ITO	70	10^3	10^5	5655	167
$Ti/PdSe_2/Au$	3	10^3	10^5	100	115
Cr/CuSe/Au	2.4	100	10^6	300	110
$Ag/HfO_x/Pt$	300	10^3	10^4	100	168
$Ag/CuInSe_2/Mo$	400	4×10^5	10^4	160	169
$Ag/Ag_2S/Ag$	100	10^2	10^4	10^5	170
$Ag/STO{:}Ag/SiO_2/p^{++}$-Si	70	10^3	10^4	10^3	16
$Ag/CeO_2/Pt$	27	4	5×10^4	100	171
$Ta/Ta_2O_5/ZrO_2/Pt$	12	10^2	10^4	10^4	172
Al/polymer membrane/ITO	300	10^3	10^4	20	173
Al/hollow MEH-PPV/2D CMP/ITO	45	10^5	3×10^4	50	174
Ag/CS-rGO/ITO/PET	80	10^3	10^4	100	143
Ag/fluoropolymer/Au	280	10^5	2000	400	146
Ag/PEI/Pt	400	10^5	10^5	1000	145

but most of the neural networks fabricated so far do not meet the theoretical requirements. In other words, the neural networks can imitate the bio-synaptic function of the human brain to a certain extent, but the integrated array size is still not large enough, and the integration density is not high enough, thus hindering the practical application of memristor-based neural networks. There are two main reasons for the difficulties in the large-scale integration of memristors. One is that the

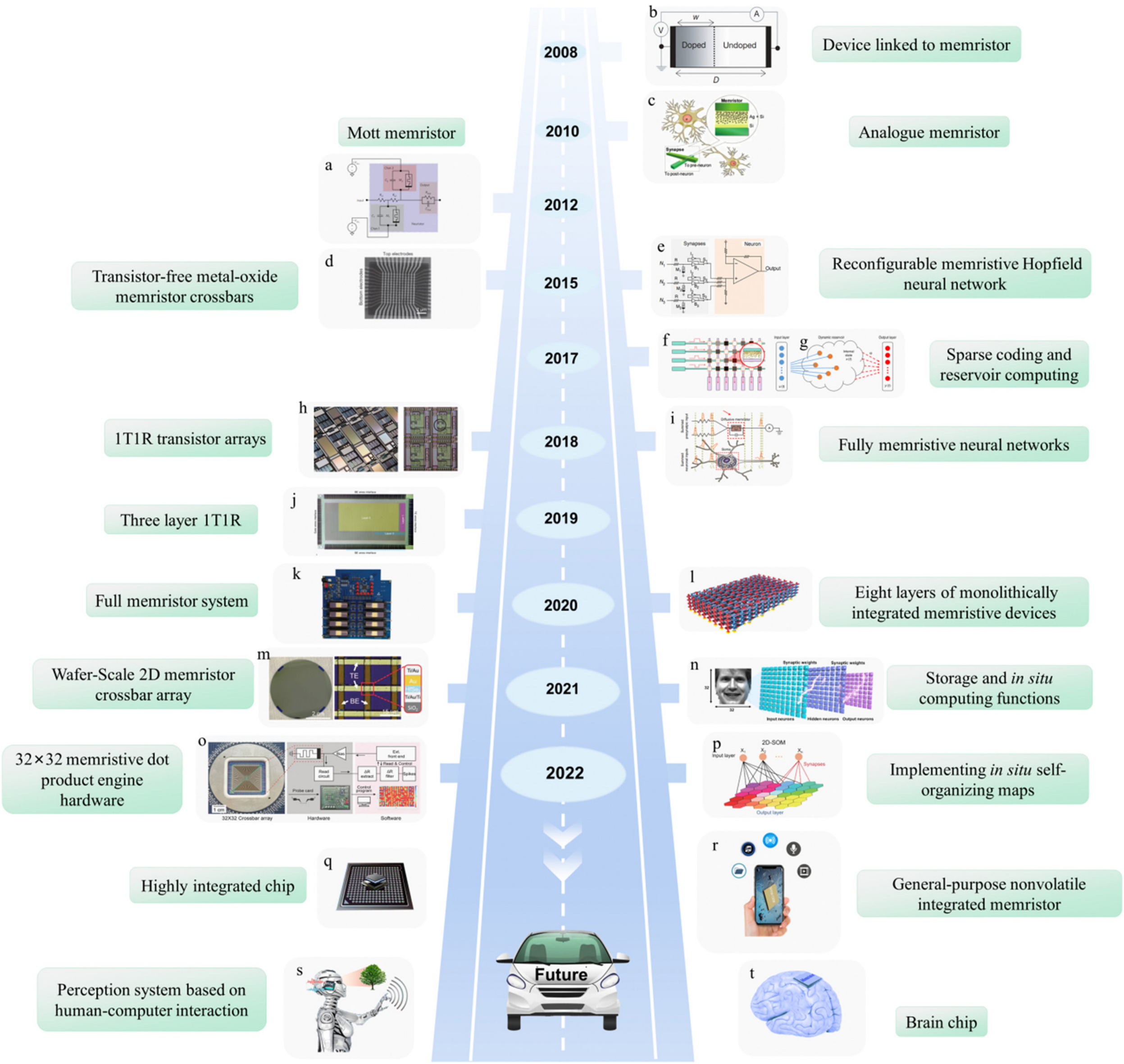

Fig. 16 The development roadmap and future work trend for memristor-based neural networks for neuromorphic computing and artificial intelligence applications. (a) Mott memristor. Panel a is reproduced with permission.[181] Copyright 2012, Nature Publishing Group. (b) A device linked to the memristor. Panel b is reproduced with permission.[2] Copyright 2008, Nature Publishing Group. (c) An analogue memristor. Panel c is reproduced with permission.[153] Copyright 2010, American Chemical Society. (d) An integrated 12 × 12 crossbar. Panel d is reproduced with permission.[182] Copyright 2015, Nature Publishing Group. (e) A reconfigurable memristive Hopfield neural network. Panel e is reproduced with permission.[183] Copyright 2015, Nature Publishing Group. (f) Sparse coding. Panel f is reproduced with permission.[184] Copyright 2017, Nature Publishing Group. (g) Reservoir computing. Panel g is reproduced with permission.[185] Copyright 2017, Nature Publishing Group. (h) A 1T1R transistor array. Panel h is reproduced with permission.[186] Copyright 2018, Nature Publishing Group. (i) Fully memristive neural networks. Panel i is reproduced with permission.[187] Copyright 2018, Nature publishing Group. (j) A three-layer 1T1R. Panel j is reproduced with permission.[188] Copyright 2019, Nature Publishing Group. (k) A full memristor system. Panel k is reproduced with permission.[85] Copyright 2020, Nature Publishing Group. (l) The eight layers of monolithically integrated memristive devices. Panel l is reproduced with permission.[189] Copyright 2020, Nature Publishing Group. (m) A wafer-scale 2D memristor crossbar array. Panel m is reproduced with permission.[114] Copyright 2022, Wiley-VCH. (n) Storage and *in situ* computing functions. Panel n is reproduced with permission.[86] Copyright 2021, Elsevier. (o) A 32 × 32 crossbar array. Panel o is reproduced with permission.[87] Copyright 2022, Wiley-VCH. (p) Implementing *in situ* self-organizing maps. Panel p is reproduced with permission.[190] Copyright 2022, Nature Publishing Group. (q) A highly integrated chip. (r) A general-purpose nonvolatile integrated memristor. (s) A perception system based on human-computer interaction. (t) A brain chip.

integration of large-scale memristor devices into the crossbar array to form a high-density memristor matrix can increase the parasitic line resistance of the crossbar array, thus greatly reducing the calculation accuracy of the memristor-based neural networks. On the other hand, the integrated crossbar array of the memristors may have a problem in interaction, which makes programming very difficult. In addition, the variations in material design and process methods involved in the process of manufacturing memristive devices further affect performance uniformity and the stability of the memristor arrays.

At present, although some 2D materials with high crystallinity can be fabricated *via* exfoliation techniques, it is still challenging to prepare 2D materials with large areas and uniform physical properties. The synthesis methods and transfer techniques for industrial-scale production still need to be improved for large-area and high-quality 2D materials. Most 2D semiconductors easily react or oxidize under ambient conditions, resulting in the degradation of device performance. For some other memristors, such as the Hewlett-Packard memristor, although several mechanisms have been proposed to explain the behavior of the memristor; however, the exact explanation is not uniform enough, and the underlying cause of the memristive effect has not yet been completely discovered. Therefore, finding a reliable and in-depth theory to understand and optimize the memristive effect has become an urgent issue. In addition, the compatibility of the memristors with existing CMOS fabrication processes has also become another limiting factor for the development of memristor-based brain-like chips. Therefore, more efforts are needed in material design, nanostructure manipulation, film homogeneity, stability, and fundamental physical properties in order to further develop the application of memristor-based neural networks in artificial intelligence.

One of the ways to solve the integration challenge is to use three-dimensional (3D) stacked memory devices to reduce the parasitic line resistance of each individual layer. Since cognitive operations in high-dimensional spaces rely on a large number of weights, they naturally require high memory density. Therefore, 3D vertical stacking of memory beams may be advantageous in terms of integrated density per unit area. The summary and comparison of some representative memristors based on different materials are shown in Table 1. It is believed that the variability problem can be solved by reducing the memory unit size, for example, the most advanced memory feature size is about 10 nm. In addition, the change in the resistive switching characteristics of the memristive device is related to the randomness of the conductive filament in the formation process. Theoretically, this can be avoided when the size of the memristor is reduced to the atomic level. In practice, if the size of the memristor is further reduced, it is possible to limit the filament to a smaller volume so as to better adjust the number and shape of the filaments. It should be considered that a single conductive filament comparable to the device size not only improves the uniformity of device performance, but also reduces the size of the memristive device, which eventually reduces the programming current requirement of the memristor unit, thereby significantly reducing power consumption.

Memristor-based artificial neural networks are discussed in terms of materials, device structure, operating mechanism, and application scope. As shown in Fig. 16, since the discovery of memristive materials, a great variety of materials have been used for the fabrication of memristive devices ranging from inorganic materials, organic materials, and inorganic-organic hybrid materials. The memristors based on inorganic materials are covered with traditional oxide materials, insulating hexagonal BN, transition metal sulfides, 2D-MXenes materials, ferroelectric materials, *etc.* Organic materials, including natural materials such as proteins, carbohydrates, DNA, fibers, and organic polymers, have also been applied for the preparation of memristive devices.[175] An extensive range of materials, including 0-dimensional, 1-dimensional, 2-dimensional and 3-dimensional materials, have been employed. At present, the major route to developing memristive materials is to improve material synthesis methods and broaden the material systems.[176–180] This is mainly reflected in optimizing the preparation and growth of materials. On the other hand, it is necessary to continuously improve the interface effect of materials and conduct more in-depth research on the special properties of materials in different dimensions. Furthermore, at the network construction level, it is essential to continuously optimize the algorithm hardware design to improve the integration density of the memristive devices and the stability between memristors.

In summary, we have reviewed in detail the technologies relevant to the integration of neural networks based on memristors, from the materials used for preparing memristors and various advanced applications of neural networks to the future prospects of artificial intelligence. At the same time, the types of functional materials commonly used in memristors and their working mechanisms are analyzed comprehensively. In particular, the important characteristics of 2D materials and ferroelectric materials used to fabricate memristive devices and the mechanisms of the polymorphic memory phenomena in resistive-switching devices are summarized. In addition, this review also discusses the development status, basic operating principles and key challenges of the latest technology and the application of memristor-based neural networks in neuromorphic computing. Furthermore, some scalable applications based on memristive neural networks, including memory computing, logic computing and logic display, are also discussed. Therefore, this review systematically summarizes the extensive research on neural networks based on memristors to achieve the application of optimized memristors and more energy-efficient neuromorphic computing systems for advanced artificial intelligence.

Conflicts of interest

The authors declare no competing financial interest.

Acknowledgements

The authors gratefully acknowledge financial support from the Fundamental Research Funds for the Central Universities

(Grant No. 2682021CX076), the National Key R&D Program of China (No. 2017YFE0301401), and B. Sun is grateful to the Xi'an Jiaotong University for the financial support of the young talent project.

References

1 L. Chua, *IEEE Trans. Circuit Theory*, 1971, **18**, 507–519.
2 D. B. Strukov, G. S. Snider, D. R. Stewart and R. S. Williams, *Nature*, 2008, **453**, 80–83.
3 P. Hou, J. Wang, X. Zhong and Y. Wu, *RSC Adv.*, 2016, **6**, 54113–54118.
4 H. Yildirim and R. Pachter, *ACS Appl. Electron. Mater.*, 2019, **1**, 467–477.
5 C. Hsu, Y. Wang, C. Wan, I. Wang, C. Chou, W. Lai, Y. Lee and T. Hou, *Nat. Nanotechnol.*, 2014, **25**, 165202.
6 R. Waser and M. Aono, *Nat. Mater.*, 2007, **6**, 833–840.
7 M. K. Akbari and S. Zhuiykov, *Nat. Commun.*, 2019, **10**, 3873.
8 M. Kumar, H. S. Kim and J. Kim, *Adv. Mater.*, 2019, **31**, 1900021.
9 Y. Ren, L. Hu, J.-Y. Mao, J. Yuan, Y.-J. Zeng, S. Ruan, J.-Q. Yang, L. Zhou, Y. Zhou and S.-T. Han, *J. Mater. Chem. C*, 2018, **6**, 9383–9393.
10 L. Fan, Y. Chen, Q. Liu, S. Chen, L. Zhu, Q. Meng, B. Wang, Q. Zhang, H. Ren and C. Zou, *ACS Appl. Mater. Interfaces*, 2016, **8**, 32971–32977.
11 K. Liu, L. Qin, X. Zhang, J. Zhu, X. Sun, K. Yang, Y. Cai, Y. Yang and R. Huang, *Faraday Discuss.*, 2019, **213**, 41–52.
12 Y. Yang, X. Zhang, L. Qin, Q. Zeng., X. Qin and R. Huang, *Nat. Commun.*, 2017, **8**, 15173.
13 Z. Shen, Y. Qi, I. Z. Mitrovic, C. Zhao, S. Hall, L. Yang, T. Luo, Y. Huang and C. Zhao, *Micromachines*, 2019, **10**, 446.
14 Y. Goh and S. Jeon, *Nanotechnology*, 2018, **29**, 335201.
15 Z. Xiao and J. Huang, *Adv. Electron. Mater.*, 2016, **2**, 1600100.
16 N. Ilyas, J. Wang, C. Li, H. Fu, D. Li, X. Jiang, D. Gu, Y. Jiang and W. Li, *J. Mater. Sci. Technol.*, 2022, **97**, 254–263.
17 C. Papakonstantinopoulos, P. Bousoulas, M. Tsigkourakos, D. Sakellaropoulos, L. Sygellou and D. Tsoukalas, *ACS Appl. Nano Mater.*, 2021, **3**, 2729–2737.
18 P. Bousoulas, D. Sakellaropoulos and D. Tsoukalas, *Appl. Phys. Lett.*, 2021, **118**, 143502.
19 Y. X. Yu, L. Pan, M.-K. Son, M. L. Mayer, W.-D. Zhang, A. Hagfeldt, J. Luo and M. Grätzel, *ACS Energy Lett.*, 2018, **3**, 760–766.
20 J. Bera, A. Betal, A. Sharma, U. Shankar, A. K. Rath and S. Sahu, *ACS Appl. Nano Mater.*, 2022, **5**, 8502–8510.
21 X. Zhao, H. Xu, Z. Wang, Y. Li and Y. Liu, *InfoMat*, 2019, **1**, 183–210.
22 M. K. Mojadidi, P. Kumar, A. N. Mahmoud, I. Y. Elgendy, H. Shapiro, B. West, A. C. Charles, H. P. Mattle, S. Sorensen, B. Meier, S. D. Silberstein and J. M. Tobis, *J. Am. Coll. Cardiol.*, 2021, **77**, 667–676.
23 S. Ren, L. Tang, Q. Sun, Z. Li, H. Yang and W. Chen, *J. Alloys Compd.*, 2018, **763**, 638–642.
24 S. Anwarhussaini, H. Battula, P. K. R. Boppidi, S. Kundu, C. Chakraborty and S. Jayanty, *Org. Electron.*, 2020, **76**, 105457.
25 C.-H. Hsu, J.-S. Lin, Y.-D. He, S.-F. Yang, P.-C. Yang and W. S. Chen, *Thin Solid Films*, 2011, **519**, 5033–5037.
26 J. Xiao, W. L. Ong, Z. Guo, G. W. Ho and K. Zeng, *ACS Appl. Mater. Interfaces*, 2015, **7**, 11412–11422.
27 C. Li, C. E. Graves, X. Sheng, D. Miller, M. Foltin, G. Pedretti and J. P. Strachan, *Nat. Commun.*, 2020, **11**, 1638.
28 Q. Cao, W. Lü, X. R. Wang, X. Guan, L. Wang, X. Guan, L. Wang, S. Yan, T. Wu and X. Wang, *ACS Appl. Mater. Interfaces*, 2020, 12, 42449–42471.
29 L. Minati, L. V. Gambuzza, W. J. Thio, J. C. Sprott and M. Frasca, *Chaos Soliton. Fract.*, 2020, **138**, 109990.
30 L. Sun, Z. Wang, J. Jiang, Y. Kim, B. Joo, S. Zheng, S. Lee, W. J. Yu, B. S. Kong and H. Yang, *Sci. Adv.*, 2021, **7**, eabg1455.
31 W. Yao, C. Wang, Y. Sun, C. Zhou and H. Lin, *App. Math. Comput.*, 2020, **386**, 125483.
32 S. Pi, C. Li, H. Jiang, W. Xia, H. Xin, J. J. Yang and Q. Xia, *Nat. Nanotechnol.*, 2019, **14**, 35–39.
33 Z. Wang, M. Rao, R. Midya, S. Joshi, H. Jiang, P. Lin, W. Song, S. Asapu, Y. Zhuo, C. Li, H. Wu, Q. Xia and J. J. Yang, *Adv. Funct. Mater.*, 2018, **28**, 1704862.
34 S. Yu, B. Gao, Z. Fang, H. Yu, J. Kang and H.-S. P. Wong, *Adv.Mater.*, 2013, **25**, 1774–1779.
35 L. Cheng, Y. Li, K.-S. Yin, S.-Y. Hu, Y.-T. Su, M.-M. Jin, Z.-R. Wang, T.-C. Chang and X.-S. Miao, *Adv. Funct. Mater.*, 2019, **29**, 1905660.
36 W. Zhang, B. Gao, J. Tang, P. Yao, S. Yu, M.-F. Chang, H.-J. Yoo, H. Qian and H. Wu, *Nat. Electron.*, 2020, **3**, 371–382.
37 K. Wang, J. Chen and X. Yan, *Nano Energy*, 2021, **79**, 105453.
38 M. Zhao, S. Wang, D. Li, R. Wang, F. Li, M. Wu, K. Liang, H. Ren, X. Zheng, C. Guo, X. Ma, B. Zhu, H. Wang and Y. Hao, *Adv. Electron. Mater.*, 2022, **8**, 2101139.
39 B. Sun, T. Guo, G. Zhou, J. Wu, Y. Chen, Y. N. Zhou and Y. A. Wu, *ACS Appl. Bio. Mater.*, 2021, **4**, 1976–1985.
40 D. Ielmini and G. Pedretti, *Adv. Intell. Syst.*, 2020, **2**, 2000040.
41 S. Seo, J.-H. Lee, R.-G. Lee, T.-H. Kim, S. Park, S. Jung, H.-K. Lee, M. Andreev, K.-B. Lee, K.-S. Jung, S. Oh, H.-J. Lee, K. S. Kim, G. Y. Yeom, Y.-H. Kim and J.-H. Park, *Adv. Mater.*, 2021, **33**, e2102980.
42 S. Oh, J.-H. Lee, S. Seo, H. Choo, D. Lee, J.-I. Cho and J.-H. Park, *Adv. Sci.*, 2022, **9**, e2103808.
43 P. Pfeiffer, I. L. Egusquiza, M. D. Ventra, M. Sanz and E. Solano, *Sci. Rep.*, 2016, **426**, 29507.
44 S. Mao, X. Zhang, G. Zhou, Y. Chen, C. Ke, W. Zhou, B. Sun and Y. Zhao, *ACS Appl. Electron. Mater.*, 2021, **3**, 5537–5547.
45 M. Spagnolo, J. Morris, S. Piacentini, M. Antesberger, F. Massa, A. Crespi, F. Ceccarelli, R. Osellame and P. Walther, *Nat. Photonics*, 2022, **16**, 318–323.

46 S. Oh, H. Hwang and I. K. Yoo, *APL Mater.*, 2019, **7**, 091109.
47 S. Yu, *Proc. IEEE*, 2018, **106**, 260–285.
48 D. Silver, A. Huang and C. J. Maddison, *et al.*, *Nature*, 2016, **529**, 484–489.
49 D. S. Jeong, K. M. Kim, S. Kim, B. J. Choi and C. S. Hwang, *Adv. Electron. Mater.*, 2016, **2**, 1600090.
50 B. J. Choi, A. C. Torrezan, J. P. Strachan, P. G. Kotula, A. J. Lohn, M. J. Marinella, Z. Li, R. S. Williams and J. J. Yang, *Adv. Funct. Mater.*, 2016, **26**, 5290.
51 Y. LeCun, Y. Bengio and G. Hinton, *Nature*, 2015, **521**, 436–444.
52 J. Meng, T. Wang, H. Zhu, L. Ji, W. Bao, P. Zhou, L. Chen, Q.-Q. Sun and W. Zhang, *Nano Lett.*, 2022, **22**, 81–89.
53 H. Tan, Y. Zhou, Q. Tao, J. Rosen and S. V. Dijken, *Nat. Commun.*, 2021, **12**, 1120.
54 K. Roy, A. Jaiswal and P. Panda, *Nature*, 2019, **575**, 607–617.
55 Q. Xia and J. J. Yang, *Nat. Mater.*, 2019, **18**, 309–323.
56 Y. Zhang, Z. R. Wang, J. D. Zhu, Y. C. Yang, M. Y. Rao, W. H. Song, Y. Zhuo, X. M. Zhang, M. L. Cui, L. L. Shen, R. Huang and J. J. Yang, *Appl. Phys. Rev.*, 2020, **7**, 011308.
57 Y. Yang, B. Chen and W. D. Lu, *Adv. Mater.*, 2015, **27**, 7720–7727.
58 J.-L. Meng, T.-Y. Wang, Z.-Y. He, L. Chen, H. Zhu, L. Ji, Q.-Q. Sun, S.-J. Ding, W.-Z. Bao, P. Zhou and D. W. Zhang, *Mater. Horiz.*, 2021, **8**, 538–546.
59 Y. Park and J.-S. Lee, *ACS Appl. Mater. Interfaces*, 2017, **9**, 6207–6212.
60 B. Sun, G. Zhou, L. Sun, H. Zhao, Y. Chen, F. Yang, Y. Zhao and Q. Song, *Nanoscale Horiz.*, 2021, **6**, 939–970.
61 G. Goh, N. Cammarata, C. Voss, S. Carter, M. Petrov, L. Schubert, A. Radford and C. Olah, *Distill*, 2021, **6**, e30.
62 S. Mangini, F. Tacchino, D. Gerace, D. Bajoni and C. Macchiavello, *Europhys. Lett.*, 2021, **134**, 10002.
63 U. Hasson, S. A. Nastase and A. Goldstein, *Neuron*, 2020, **105**, 416–434.
64 D. Beniaguev, I. Segev and M. London, *Neuron*, 2021, **109**, 2727–2739.
65 S. Y. Chung and L. F. Abbott, *Curr. Opin. Neurobiol.*, 2021, **70**, 137–144.
66 F. Hu, Y. Zhu, J. Liu and L. Li, *Appl. Soft Comput.*, 2020, **91**, 106218.
67 A. Xu, H. Chang, Y. Xu, R. Li, X. Li and Y. Zhao, *Waste Manage.*, 2021, **124**, 385–402.
68 A. Krogh, *Nat. Biotechnol.*, 2008, **26**, 195–197.
69 G. R. Yang and X.-J. Wang, *Neuron*, 2020, **107**, 1048–1070.
70 Q. Zhang, H. Yu, M. Barbiero, B. Wang and M. Gu, *Light: Sci. Appl.*, 2019, **8**, 1–14.
71 X. Li, J. Tang, Q. Zhang, B. Gao, J. J. Yang, S. Song, W. Wu, W. Zhang, P. Yao, N. Deng, L. Deng, Y. Xie, H. Qian and H. Wu, *Nat. Nanotechnol.*, 2020, **15**, 776–782.
72 T. Zhang, X. Cheng, S. Jia, M.-M. Poo, Y. Zeng and B. Xu, *Sci. Adv.*, 2021, **7**, eabh0146.
73 W. Liu, Z. Wang, X. Liu, N. Zeng, Y. Liu and F. E. Alsasdi, *Neurocomputing*, 2017, **234**, 11–26.
74 N. Kriegeskorte and T. Golan, *Curr. Biol.*, 2019, **29**, R231–R236.
75 Q. Cheng, H. Li, Q. Wu and K. N. Ngan, *Neurocomputing*, 2020, **388**, 78–89.
76 A. Rahimian, M. R. Hosseini, I. Martek, A. Taroun, A. Alvanchi and I. Odeh, *Automat. Constr.*, 2022, **139**, 104268.
77 Y. Lecun, L. Bottou, Y. Bengio and P. Haffner, *Proc. IEEE*, 1998, **86**, 2278–2324.
78 W. Poole, *Nat. Mach. Intell.*, 2022, **4**, 614–615.
79 I. A. Mustafina, V. Ishmetov, N. Zagidullin and I. V. Buzaev, *J. Am. Coll. Cardiol.*, 2022, **79**, S34–S34.
80 P. Thai, S. Alam, N. Lilith and B. T. Nguyen, *Transport. Res. C-EMER*, 2022, **137**, 103590.
81 L. Zhou and X. Gu, *Neural Networks*, 2020, **121**, 308–318.
82 J. Peng, X. Mei, W. Li, L. Hong, B. Sun and H. Li, *Remote. Sens*, 2021, **13**, 742.
83 M. Hu, C. E. Graves, C. Li, Y. Li, N. Ge, E. Montgomery, N. Davila, H. Jiang, R. S. Williams, J. J. Yang, Q. Xia and J. P. Strachan, *Adv. Mater.*, 2018, **30**, 1705914.
84 Y. Lin, C. Wang, Y. Ren, Z. Wang, H. Xu, X. Zhao, J. Ma and Y. Liu, *Small Methods*, 2019, **3**, 1900160.
85 P. Yao, H. Wu, B. Gao, J. Tang, Q. Zhang, W. Zhang, J. J. Yang and H. Qian, *Nature*, 2020, **577**, 641–646.
86 T.-Y. Wang, J.-L. Meng, Q.-X. Li, Z.-Y. He, H. Zhu, L. Ji, Q.-Q. Sun, L. Chen and D. W. Zhang, *Nano Energy*, 2021, **89**, 106291.
87 W. H. Cheong, J. B. Jeon, J. H. In, G. Kim, H. Song, J. An, J. Park, Y. S. Kim, C. S. Hwang and K. M. Kim, *Adv. Funct. Mater.*, 2022, **32**, 2200337.
88 C. Li, M. Hu, Y. Li, H. Jiang, N. Ge, E. Montgomery, J. Zhang, W. Song, N. Dávila, C. E. Graves, Z. Li, J. P. Strachan, P. Lin, Z. Wang, M. Barnell, Q. Wu, R. S. Williams, J. J. Yang and Q. Xia, *Nat. Electron.*, 2018, **1**, 52–59.
89 K. Wang, Q. Hu, B. Gao, Q. Lin, F.-W. Zhuge, D.-Y. Zhang, L. Wang, Y.-H. He, R. H. Scheicher, H. Tong and X.-S. Miao, *Mater. Horiz.*, 2021, **8**, 619–629.
90 J. M. Lopez, Q. Rafhay, M. Dampfhoffer, L. Reganaz, N. Castellani, V. Meli, S. Martin, L. Grenouillet, G. Navarro, T. Magis, C. Carabasse, T. Hirtzlin, E. Vianello, D. Deleruyelle, J. Portal, G. Molas and F. Andrieu, *Adv. Electron. Mater.*, 2022, **8**, 2200323.
91 W. Huh, S. Jang, J. Y. Lee, D. Lee, J. M. Lee, H.-G. Park, J. C. Kim, H. Y. Jeong, G. Wang and C.-H. Lee, *Adv. Mater.*, 2018, **30**, 1801447.
92 Y. Song, J. Liu, W. Li, L. Liu, L. Yang, S. Lei and W. Hu, *Chem. Commun.*, 2020, **56**, 6356–6359.
93 J. Chai, S. Tong, C. Li, C. Manzano, B. Li, Y. Liu, M. Lin, L. Wong, J. Cheng, J. Wu, A. Lau, Q. Xie, S. J. Pennycook, H. Medina, M. Yang, S. Wang and D. Chi, *Adv. Mater.*, 2020, **32**, 2002704.
94 W. Li, J. Liu, Y. Yu, G. Feng, Y. Song, Q. Liang, L. Liu, S. Lei and W. Hu, *Mater. Chem. Front.*, 2020, **4**, 1268–1273.
95 R. D. Nikam, K. G. Rajput and H. Hwang, *Small*, 2021, **17**, 2006760.
96 G. Rachmuth, H. Z. Shouval, M. F. Bear and C.-S. Poon, *Proc. Natl. Acad. Sci. U. S. A.*, 2011, **108**, E1266–E1274.

97 T. Ohno, T. Hasegawa, T. Tsuruoka, K. Terabe, J. K. Gimzewski and M. Aono, *Nat. Mater.*, 2011, **10**, 591–595.
98 Y. Zeng, X. Du, Y. Li, Y. Guo, Y. Xie, J. Huang, G. Rao, Y. Liu, T. Lei, C. Gong, X. Wang and B. Sun, *J. Alloys Compd.*, 2021, **869**, 159335.
99 M. Zhang, Q. Qin, X. Chen, R. Tang, A. Han, S. Yao, R. Dan, Q. Wang, Y. Wang, H. Gu, H. Zhang, E. Hu, L. Wang, J. Xu and Y. Tong, *Ceram. Int.*, 2022, **48**, 16263–16272.
100 A. Sokolov, M. Ali, H. Li, Y.-R. Jeon, M. J. Ko and C. Choi, *Adv. Electron. Mater.*, 2021, **7**, 2000866.
101 Y. Wang, Y. Gong, L. Yang, Z. Xiong, Z. Lv, X. Xing, Y. Zhou, B. Zhang, C. Su, Q. Liao and S.-T. Han, *Adv. Funct. Mater.*, 2021, **31**, 2100144.
102 X. Zhang, S. Wu., R. Yu, E. Li, D. Liu, C. Gao, Y. Hu, T. Guo and H. Chen, *Matter*, 2022, **5**, 3023–3040.
103 F. Wan, Q. Wang, T. Harumoto, T. Gao, K. Ando, Y. Nakamura and J. Shi, *Adv. Funct. Mater.*, 2020, **30**, 2007101.
104 A. K. Jena, M. C. Sahu, K. U. Mohanan, S. K. Mallik, S. Sahoo, G. K. Pradhan and S. Sahoo, *ACS Appl. Mater. Interfaces*, 2023, **15**, 3573–3585.
105 Q. Gao, A. Huang, J. Zhang, Y. Ji, J. Zhang, X. Chen, X. Geng, Q. Hu, M. Wang, Z. Xiao and P. K. Chu, *NPG Asia Mater.*, 2021, **13**, 1–10.
106 A. K. Parit, M. S. Yadav, A. K. Gupta, A. Mikhaylov and B. Rawat, *Chaos, Solitons Fractals*, 2021, **145**, 110818.
107 F. Zeng, Y. Guo, W. Hu, Y. Tan, Z. Zhang, J. Feng and X. Tang, *ACS Appl. Mater. Interfaces*, 2020, **12**, 23094–23101.
108 R. A. John, N. Shah, S. K. Vishwanath, S. E. Ng, B. Febriansyah, M. Jagadeeswararao, C.-H. Chang, A. Basu and N. Mathews, *Nat. Commun.*, 2021, **12**, 1–11.
109 R. Xu, H. Jang, M.-H. Lee, D. Amanov, Y. Cho, H. Kim, S. Park, H.-J. Shin and D. Ham, *Nano Lett.*, 2019, **19**, 2411–2417.
110 L. Yin, R. Cheng, Y. Wen, B. Zhai, J. Jiang, H. Wang, C. Liu and J. He, *Adv. Mater.*, 2022, **34**, 2108313.
111 A. Bala, B. So, P. Pujar, C. Moon and S. Kim, *ACS Nano*, 2023, **17**, 4296–4305.
112 X. F. Liu, Y. Zhang, N. Wang, S. Luo, K. Peng, L. Wang, H. Chen, W. Gao, X. H. Chen, Y. Bao, G. Liang and K. P. Loh, *Nano Lett.*, 2021, **21**, 8800–8807.
113 L. Liu, Y. Li, X. Huang, J. Chen, Z. Yang, K.-H. Xue, M. Xu, H. Chen, P. Zhou and X. Miao, *Adv. Sci.*, 2021, **8**, 2005038.
114 S. Li, M.-E. Pam, Y. Li, L. Chen, Y.-C. Chien, X. Fong, D. Chi and K.-W. Ang, *Adv. Mater.*, 2022, **34**, 2103376.
115 Y. Li, L. Loh, S. Li, L. Chen, B. Li, M. Bosman and K.-W. Ang, *Nat. Electron.*, 2021, **4**, 348–356.
116 S. Chen, M. R. Mahmoodi, Y. Shi, C. Mahata, B. Yuan, X. Liang, C. Wen, F. Hui, D. Akinwande, D. B. Strukov and M. Lanza, *Nat. Electron.*, 2020, **3**, 638–645.
117 P. Kumar, C. S. Thakur, K. Zhu, X. Gao, S.-D. Wang and M. Lanza, *Npj 2D Mater. Appl.*, 2022, **6**, 1–10.
118 J.-Y. Mao, S. Wu, G. Ding, Z.-P. Wang, F.-S. Qian, J.-Q. Yang, Y. Zhou and S.-T. Han, *Small*, 2022, **18**, 2106253.
119 S. J. Yang, M. M. Dahan, O. Levit, F. Makal, P. Peterson, J. Alikpala, S. T. Nibhanupudi, C. J. Luth, S. K. Banerjee, M. Kim, A. Roessler, E. Yalon and D. Akinwande, *Nano Lett.*, 2023, **23**, 1152–1158.
120 J. Y. Park, D.-H. Choe, D. H. Lee, G. T. Yu, K. Yang, S. H. Kim, G. H. Park, S.-G. Nam, H. J. Lee, S. Jo, B. J. Kuh, D. Ha, Y. Kim, J. Heo and M. H. Park, *Adv. Mater.*, 2023, 2204904, DOI: **10.1002/adma.202204904**.
121 S. Baek, H. H. Yoo, J. H. Ju, P. Sriboriboon, P. Singh, J. Niu, J.-H. Park, C. Shin, Y. Kim and S. Lee, *Adv. Sci.*, 2022, **9**, 2200566.
122 X. Niu, B. Tian, Q. Zhu, B. Dkhil and C. Duan, *Appl. Phys. Rev.*, 2022, **9**, 021309.
123 A. R. Jayakrishnan, A. Kumar, S. Druvakumar, R. John, M. Sudeesh, V. S. Puli, J. P. B. Silva, M. J. M. Gomesfg and K. C. Sekhar, *J. Mater. Chem. C*, 2023, **11**, 827–858.
124 Y.-Y. Tang, J.-C. Liu, Y.-L. Zeng, H. Peng, X.-Q. Huang, M.-J. Yang and R.-G. Xiong, *J. Am. Chem. Soc.*, 2021, **143**, 13816–13823.
125 W.-Q. Liao, B.-B. Deng, Z.-X. Wang, T.-T. Cheng, Y.-T. Hu, S.-P. Cheng and R.-G. Xiong, *Adv. Sci.*, 2021, **8**, 2102614.
126 M. Gabel and Y. Gu, *Adv. Funct. Mater.*, 2021, **31**, 2009999.
127 F. Xue, X. He, Z. Wang, J. R. D. Retamal, Z. Chai, L. Jing, C. Zhang, H. Fang, Y. Chai, T. Jiang, W. Zhang, H. N. Alshareef, Z. Ji, L.-J. Li, J.-H. He and X. Zhang, *Adv. Mater.*, 2021, **33**, 2008709.
128 F. Xue, X. He, Y. Ma, D. Zheng, C. Zhang, L.-J. Li, J.-H. He, B. Yu and X. Zhang, *Nat. Commun.*, 2021, **12**, 1–8.
129 X. Yan, H. He, G. Liu, Z. Zhao, Y. Pei, P. Liu, J. Zhao, Z. Zhou and K. Wang, *Adv. Mater.*, 2022, **18**, 2110343.
130 W.-M. Zhong, X.-G. Tang, Q.-X. Liu and Y.-P. Jiang, *Mater. Des.*, 2022, **222**, 111046.
131 Z. Luo, Z. Wang, Z. Guan, C. Ma, L. Zhao, C. Liu, H. Sun, H. Wang, Y. Lin and X. Jin, *Nat. Commun.*, 2022, **13**, 1–11.
132 Z. Gao, Y. Wang, Z. Lv, P. Xie, Z.-X. Xu, M. Luo, Y. Zhang, S. Huang, K. Zhou, G. Zhang, G. Duan, Y. Zhou and S.-T. Han, *Appl. Phys. Rev.*, 2022, **9**, 021417.
133 Y. Cai, J. Zhang, M. Yan, Y. Jiang, H. Jawad, B. Tian, W. Wang, Y. Zhan, Y. Qin, S. Xiong, C. Cong, Z.-J. Qiu, C. Duan, R. Liu and L. Hu, *Npj Flexible Electron.*, 2022, **6**, 1–9.
134 J. Wang, B. Sun, G. Zhou, S. Zhu, C. Yang, C. Ke, Y. Zhao and H. Wang, *J. Alloys Compd.*, 2023, **939**, 168761.
135 Z. Liu, H. Wang, M. Li, L. Tao, T. R. Paudel, H. Yu, Y. Wang, S. Hong, M. Zhang, Z. Ren, Y. Xie, E. Y. Tsymbal, J. Chen, Z. Zhang and H. Tian, *Nature*, 2023, **613**, 656–661.
136 H. Li, S. Geng, T. Liu, M. Cao and J. Su, *ACS Appl. Mater.*, 2023, **15**, 5456–5465.
137 R. S. Potember, T. O. Poehler and D. O. Cowan, *Appl. Phys. Lett.*, 1979, **34**, 405–407.
138 T. Fu, X. Liu, H. Gao, J. E. Ward, X. Liu, B. Yin, Z. Wang, Y. Zhuo, D. J. F. Walker, J. J. Yang, J. Chen, D. R. Lovley and J. Yao, *Nat. Commun.*, 2020, **11**, 1–10.
139 K. Chang, A. Dong, X. Yu, B. Liu, X. Zhao, R. Wang, Z. Gan, K. Jiang, Y. Niu, X. Dong, D. Zheng, Y. Li, P. Bao, Z. Zhao and H. Wang, *Adv. Electron. Mater.*, 2022, **8**, 2100843.
140 T. Hussain, H. Abbas, C. Youn, H. Lee, T. Boynazarov, B. Ku, Y.-R. Jeon, H. Han, J. H. Lee, C. Choi and T. Choi, *Adv. Mater. Technol.*, 2022, **7**, 2100744.

141 S.-Y. Min and W.-J. Cho, *Int. J. Mol. Sci.*, 2021, **22**, 773.

142 X. Zhao, J. Xu, D. Xie, Z. Wang, H. Xu, Y. Lin, J. Hu and Y. Liu, *Adv. Mater.*, 2021, **33**, 2104023.

143 B. Zhao, X. Zhao, Q. Li, X. Xun, T. Ouyang, Z. Zhang, Z. Kang, Q. Liao and Y. Zhang, *InfoMat*, 2022, **18**, e12350.

144 J. Zhou, W. Li, Y. Chen, Y.-H. Lin, M. Yi, J. Li, Y. Qian, Y. Guo, K. Cao, L. Xie, H. Ling, Z. Ren, J. Xu, J. Zhu, S. Yan and W. Huang, *Adv. Mater.*, 2021, **33**, 2006201.

145 D. Yang, H. Yang, X. Guo, H. Zhang, C. Jiao, W. Xiao, P. Guo, Q. Wang and D. He, *Adv. Funct. Mater.*, 2020, **30**, 2004514.

146 M.-H. Kim, H.-L. Park, M.-H. Kim, J. Jang, J.-H. Bae, I. M. Kang and S.-H. Lee, *npj Flexible Electron.*, 2021, **5**, 1–8.

147 B. Sun, J. H. L. Ngai, G. Zhou, Y. Zhou and Y. Li, *ACS Appl. Mater. Interfaces*, 2022, **14**, 41304–41315.

148 K. Zhang, Q. Xue, C. Zhou, W. Mo, C.-C. Chen, M. Li and T. Hang, *Nanoscale*, 2022, **14**, 12898–12908.

149 T. Xiong, C. Li, X. He, B. Xie, J. Zong, Y. Jiang, W. Ma, F. Wu, J. Fei and L. Mao, *Science*, 2023, **379**, 156–161.

150 M. D. Marco, M. Forti and L. Pancioni, *IEEE. Trans. Neur. Net. Lear.*, 2017, **29**, 1822–1834.

151 J. J. Yang, D. B. Strukov and D. R. Stewart, *Nat. Nanotechnol.*, 2013, **8**, 13–24.

152 Z. Q. Wang, H. Y. Xu and X. H. Li, *Adv. Funct. Mater.*, 2012, **22**, 2759–2765.

153 S. H. Jo, T. Chang, I. Ebong, B. B. Bhadviya, P. Mazumder and W. Lu, *Nano Lett.*, 2010, **10**, 1297–1301.

154 S. Kim, C. Du, P. Sheridan, W. Ma, S. Choi and W. D. Lu, *Nano Lett.*, 2015, **15**, 2203–2211.

155 C. Du, W. Ma, T. Chang, P. Sheridan and W. D. Lu, *Adv. Funct. Mater.*, 2015, **25**, 4290–4299.

156 Z. Wang, S. Joshi and S. E. Savel'ev, *Nat. Mater.*, 2017, **16**, 101–108.

157 L. Gao, Q. Ren, J. Sun, S.-T. Han and Y. Zhou, *J. Mater. Chem. C*, 2021, **9**, 16859–16884.

158 J.-U. Woo, H.-G. Hwang, S.-M. Park, T.-G. Lee and S. Nahm, *Appl. Mater. Today*, 2020, **19**, 100582.

159 X. Yan, J. Zhao, S. Liu, Z. Zhou, Q. Liu, J. Chen and X. Y. Liu, *Adv. Funct. Mater.*, 2018, **28**, 1705320.

160 J. H. Sung, J. H. Park, D. S. Jeon, D. Kim, M. J. Yu, A. C. Khot, D. T. Dongale and T. G. Kim, *Mater. Des*, 2021, **207**, 109845.

161 J. Liu, F. Yang, L. Cao, B. Li, K. Yuan, S. Lei and W. Hu, *Adv. Mater.*, 2019, **31**, 1902264.

162 C. Yin, C. Gong, S. Tian, Y. Cui, X. Wang, Y. Wang, Z. Hu, J. Huang, C. Wu, B. Chen, X. Wang and C. Li, *Adv. Funct. Mater.*, 2022, **32**, 2108455.

163 G. Kim, S. Son, H. Song, J. B. Jeon, J. Lee, W. H. Cheong, S. Choi and K. M. Kim, *Adv. Sci.*, 2023, **10**, 2205654.

164 T.-K. Su, W.-K. Cheng, C.-Y. Chen, W.-C. Wang, Y.-T. Chuang, G.-H. Tan, H.-C. Lin, C.-H. Hou, C.-M. Liu, Y.-C. Chang, J.-J. Shyue, K.-C. Wu and H.-W. Lin, *ACS Nano*, 2022, **16**, 12979–12990.

165 B. Tang, H. Veluri, Y. Li, Z. G. Yu, M. Waqar, J. F. Leong, M. Sivan, E. Zamburg, Y.-W. Zhang, J. Wang and A. V.-Y. Thean, *Nat. Commun.*, 2022, **13**, 3037.

166 J. Yu, Y. Wang, S. Qin, G. Gao, C. Xu, Z. L. Wang and Q. Sun, *Mater. Today*, 2022, **60**, 158–182.

167 R. A. John, Y. Demirağ, Y. Shynkarenko, Y. Berezovska, N. Ohannessian, M. Payvand, P. Zeng, M. I. Bodnarchuk, F. Krumeich, G. Kara, I. Shorubalko, M. V. Nair, G. A. Cooke, T. Lippert, G. Indiveri and M. V. Kovalenko, *Nat. Commun.*, 2022, **13**, 1–10.

168 Y. Wang, G. Zhou, B. Sun, W. Wang, J. Li, S. Duan and Q. Song, *J. Phys. Chem. Lett.*, 2022, **13**, 8019–8025.

169 T. Guo, K. Pan, Y. Jiao, B. Sun, C. Du, J. P. Mills, Z. Chen, X. Zhao, L. Wei, Y. N. Zhou and Y. A. Wu, *Nanoscale Horiz.*, 2022, **7**, 299–310.

170 Y. Zhu, J. Liang, X. Shi and Z. Zang, *ACS Appl. Mater. Interfaces*, 2022, **14**, 43482–43489.

171 H. Li, T. Liu, Y. Wang, S. Geng, T. Xu, M. Cao, S. Fan, T. Liu and J. Su, *Ceram. Int.*, 2022, **48**, 13754–13760.

172 M. Ismail, H. Abbas, A. Sokolov, C. Mahata, C. Choi and S. Kim, *Ceram. Int.*, 2021, **47**, 30764–30776.

173 Z. Zhang, Y. Nie, W. Hua, J. Xu, C. Ban, F. Xiu and J. Liu, *RSC Adv.*, 2020, **10**, 20900–20904.

174 Y. Yin, Z. Zhou, X. Wang, H. Mao, C. Ban, Y. Chen, J. Liu, Z. Liu and W. Huang, *ACS Appl. Mater. Interfaces*, 2019, **12**, 1103–1109.

175 S. Mao, B. Sun, G. Zhou, T. Guo, J. Wang and Y. Zhao, *Nanoscale Horiz.*, 2022, **7**, 822–848.

176 S. Zhu, B. Sun, G. Zhou, T. Guo, C. Ke, Y. Chen, F. Yang, Y. Zhang, J. Shao and Y. Zhao, *ACS Appl. Mater. Interfaces*, 2023, **15**, 5420–5431.

177 R. Gou, Z. Ouyang, C. Xu, S. He, S. Cheng, C. Shi, J. Zhao, Y. Xiao, S. Lei and B. Cheng, *Nanoscale Horiz.*, 2022, **7**, 1095–1108.

178 S. W. Cho, C. Jo, Y.-H. Kim and S. K. Park, *Nano-Micro Lett.*, 2022, **14**, 203.

179 G. Zhou, X. Ji, J. Li, F. Zhou, Z. Dong, B. Yan, B. Sun, W. Wang, X. Hu, Q. Song, L. Wang and S. Duan, *iScience*, 2022, **25**, 105240.

180 B. Sun, T. Guo, G. Zhou, S. Ranjan, Y. Jiao, L. Wei, Y. N. Zhou and Y. A. Wu, *Mater. Today Phys.*, 2021, **18**, 100393.

181 M. D. Pickett, G. M. Ribeiro and R. S. Williams, *Nat. Mater.*, 2013, **12**, 114–117.

182 M. Prezioso, F.-M. Bayat, B. D. Hoskins, G. C. Adam, K. K. Likharev and D. B. Strukov, *Nature*, 2015, **521**, 61–64.

183 S. G. Hu, Y. Liu, Z. Liu, T. P. Chen, J. J. Wang, Q. Yu, L. J. Deng, Y. Yin and S. Hosaka, *Nat. Commun.*, 2015, **6**, 1–8.

184 P. M. Sheridan, F. Cai, C. Du, W. Ma, Z. Zhang and W. D. Lu, *Nat. Nanotechnol.*, 2017, **12**, 784–789.

185 C. Du, F. Cai, M. A. Zidan, W. Ma, S. H. Lee and W. D. Lu, *Nat. Commun.*, 2017, **8**, 1–10.

186 C. Li, D. Belkin, Y. Li, P. Yan, M. Hu, N. Ge, H. Jiang, E. Montgomery, P. Lin, Z. Wang, W. Song, J. P. Strachan, M. Barnell, Q. Wu, R. S. Williams, J. J. Yang and Q. Xia, *Nature*, 2018, **9**, 1–8.

187 Z. Wang, S. Joshi, S. Savelev, W. Song, R. Midya, Y. Li, M. Rao, P. Yan, S. Asapu, Y. Zhuo, H. Jiang, P. Lin, C. Li, J. H. Yoon, N. K. Upadhyay, J. Zhang, M. Hu, J. P. Strachan, M. Barnell, Q. Wu, H. Wu, R. S. Williams, Q. Xia and J. J. Yang, *Nat. Electron.*, 2018, **1**, 137–145.

188 Z. Wang, C. Li, W. Song, M. Rao, D. Belkin, Y. Li, P. Yan, H. Jiang, P. Lin, M. Hu, J. P. Stachan, N. Ge, M. Barnell, Q. Wu, A. G. Barto, Q. Qiu, R. S. Williams, Q. Xia and J. J. Yang, *Nat. Electron.*, 2019, **2**, 115–124.

189 P. Lin, C. Li, Z. Wang, Y. Li, H. Jiang, W. Song, M. Rao, Y. Zhuo, N. K. Upadhyay, M. Barnell, Q. Wu, J. J. Yang and Q. Xia, *Nat. Electron.*, 2020, **3**, 225–232.

190 R. Wang, T. Shi, X. Zhang, J. Wei, J. Lu, J. Zhu, Z. Wu, Q. Liu and M. Liu, *Nat. Commun.*, 2022, **13**, 1–10.